ANL/ESD/12-3

Material and Energy Flows in the Materials Production, Assembly, and End-of-Life Stages of the Automotive Lithium-Ion Battery Life Cycle

Energy Systems Division

About Argonne National Laboratory
Argonne is a U.S. Department of Energy laboratory managed by UChicago Argonne, LLC under contract DE-AC02-06CH11357. The Laboratory's main facility is outside Chicago, at 9700 South Cass Avenue, Argonne, Illinois 60439. For information about Argonne and its pioneering science and technology programs, see www.anl.gov.

Availability of This Report
This report is available, at no cost, at http://www.osti.gov/bridge. It is also available on paper to the U.S. Department of Energy and its contractors, for a processing fee, from:

U.S. Department of Energy
Office of Scientific and Technical Information
P.O. Box 62
Oak Ridge, TN 37831-0062
phone (865) 576-8401
fax (865) 576-5728
reports@adonis.osti.gov

Disclaimer
This report was prepared as an account of work sponsored by an agency of the United States Government. Neither the United States Government nor any agency thereof, nor UChicago Argonne, LLC, nor any of their employees or officers, makes any warranty, express or implied, or assumes any legal liability or responsibility for the accuracy, completeness, or usefulness of any information, apparatus, product, or process disclosed, or represents that its use would not infringe privately owned rights. Reference herein to any specific commercial product, process, or service by trade name, trademark, manufacturer, or otherwise, does not necessarily constitute or imply its endorsement, recommendation, or favoring by the United States Government or any agency thereof. The views and opinions of document authors expressed herein do not necessarily state or reflect those of the United States Government or any agency thereof, Argonne National Laboratory, or UChicago Argonne, LLC.

ANL/ESD/12-3

Material and Energy Flows in the Materials Production, Assembly, and End-of-Life Stages of the Automotive Lithium-Ion Battery Life Cycle

by
J.B. Dunn,[1] L. Gaines,[1] M. Barnes,[2] J. Sullivan,[1] and M. Wang[1]
[1]Center for Transportation Research, Argonne National Laboratory
[2]Department of Mechanical Engineering, Pennsylvania State University

June 2012

CONTENTS

ACKNOWLEDGEMENTS vii

NOTATION viii

ABSTRACT 1

1 INTRODUCTION 2

2 MATERIAL INVENTORY OF BATTERIES 4

2.1 Metals 6
2.2 Active Materials, Binder, and Electrolyte 8
2.3 Plastics (Polyethylene Terephthalate, Polypropylene, and Polyethylene) 8
2.4 Electronic Parts and Temperature Control 9
2.5 Summary of Materials Inventory 9

3 MATERIAL AND ENERGY FLOW DATA AND CALCULATIONS 11

3.1 Lithium Brine and Lithium Carbonate 11
3.1.1 Soda Ash 16
3.1.2 Lime 19
3.1.3 Sulfuric Acid and Hydrochloric Acid 20
3.1.4 Alcohol 22
3.1.5 Lithium Carbonate Production in Nevada 22
3.2 Manganese Oxide 24
3.3 Lithium Manganese Oxide 26
3.4 Graphite 27
3.5 Polyvinylidene Fluoride 27
3.6 Electrolyte 28
3.7 N-Methyl-2-pyrrolidone 29
3.8 Battery Management System 30
3.9 Battery Assembly 32
3.10 Recycling Processes 34
3.10.1 Hydrometallurgical Recycling Process 35
3.10.2 Pyrometallurgical Recycling Process 43
3.10.3 Intermediate Physical Recycling Process 46
3.10.4 Direct Physical Recycling Process 49
3.10.5 Recycling Process Summary 52

CONTENTS (CONT.)

4 CONCLUSIONS AND FUTURE WORK 53

4.1 Mass Inventory of Battery Components 53
4.2 Cradle-to-Gate Inventories 53

5 REFERENCES 55

FIGURES

1 Components and Processes with Material and Energy Flows in GREET 3

2 Information Flow from Argonne Models into GREET 4

3 Cell Chemistry in a Lithium-Ion Battery 4

4 Module Structure 5

5 Lithium Brine Recovery and Concentration 12

6 Li_2CO_3 Production from Concentrated Lithium Brine 13

7 Energy Intensity of Industrial Kilns in Three Processes 25

8 Production of $LiMn_2O_4$ 26

9 Battery Manufacturing Plant Schematic 33

10 Flow Sheet of Hydrometallurgical Recycling Process 35

11 Industrial and Selected Energy Intensities for Calcining 39

12 Purchased Energy Intensity of Hydrometallurgical Process 37

13 Production Pathways of Oxidant and Leachant for Recycling Process 40

14 Pyrometallurgical Recovery Process 44

15 Intermediate Recycling Process Flowchart 47

16 Direct Recycling Process 50

TABLES

1 Battery Parameters 6

2 Material Inventories for HEV, PHEV, and BEV Batteries 10

3 Products at SQM Brine Production Facility 12

4 Material Consumption per Ton Li_2CO_3 14

5 Purchased Energy Consumption 14

6 Chilean Electricity Mix Used in GREET for Chilean-Based Processes 15

7 Raw Material and Product Transportation Distances for Li_2CO_3 Production in Chile 16

8 Purchased Energy Consumption during Soda Ash Production 17

9 Non-Combustion Air Emissions from Na_2CO_3 Production 18

10 Combustion Emission Factors for Coal-Fired Kilns 18

11 Purchased Energy Consumption during Limestone Mining and Lime Production 19

12 Non-Combustion PM Emissions during Limestone Mining 20

13 Purchased Energy Consumption during Cl_2 Production 21

14 Purchased Energy Consumption during NaCl Brine Production 22

15 Purchased Energy Consumption during Li_2CO_3 Production in Nevada 23

16 Emissions from Li_2CO_3 Production in Nevada 24

17 Emission Factors for Gas-Fired Kilns 26

18 Purchased Energy Consumption during Graphite Production 27

19 Purchased Energy Consumption during PVDF Production 27

20 Purchased Energy Consumption during $LiPF_6$ Production 28

21 Purchased Energy and Feedstock Consumption during the Production of Ethylene 28

TABLES (CONT.)

22 Purchased Energy and Materials Consumed during the Production of Ethylene Oxide 28

23 Parameters for the Production of DMC 29

24 Purchased Energy and Materials Consumed during the Production of EC 29

25 Purchased Energy Consumption during the Production of NMP 30

26 Measurements of a Battery Pack 30

27 Desktop Computer Circuit Board and Semiconductor Areas 31

28 Energy Intensity of Circuit Board and Semiconductor Production 32

29 Energy Intensity for Grinding Steps in Industrial Processes 38

30 Energy Intensity for Leaching Steps in Industrial Processes 39

31 Hydrogen Peroxide Intensity of Acid Leaching Step 40

32 Energy and Feedstock Intensity for H_2O_2 Production from Hydrogen 41

33 Energy Intensity Values for Citric Acid 42

34 Key Parameters for Pyrometallurgical Process 44

35 Purchased Energy and Material Consumption during the Smelting Process 45

36 Carbon-Containing Components in LIBs and their Carbon Contents 46

37 Material Flows in the Intermediate Physical Recycling Process 47

38 Purchased Energy Consumption during Intermediate Recycling Process 49

39 Properties of Cyclohexanone and Electrolyte 50

40 Compression Energy Demand Calculation Parameters 51

41 Purchased Energy Consumption during Direct Recycling Process 52

ACKNOWLEDGEMENTS

This research was supported by the Vehicle Technologies Program in the U.S. Department of Energy's Office of Energy Efficiency and Renewable Energy, under contract number DE-AC02-06CH11357. We would like to thank Connie Bezanson of the Vehicle Technologies Program for her support. We also acknowledge the contributions of John Molburg of Argonne National Laboratory for his analysis of energy requirements for pumping and vehicle operation at the Chemetall Foote lithium carbonate plant in Nevada and of Mark Caffarey of Umicore Group, Todd Coy of Toxco, Steve Sloop of OnTo Technology, LLC, and Tim Ellis and Jacob Hohn of RSR Corporation, who provided insight into battery recycling processes. In addition, we would like to thank the following Argonne colleagues for helpful discussions: Kevin Gallagher, Eric Rask, Aymeric Rousseau, Andy Burnham, and Dan Santini. Finally, we are grateful to Renata Arsenault of Ford Motor Company and one other anonymous reviewer for their suggestions on this report, which led to many improvements. Any errors that remain are the responsibility of the authors.

NOTATION

Argonne	Argonne National Laboratory
BACT	best available control technology
BatPaC	Battery Performance and Cost (model)
BEV	battery electric vehicle
BMS	battery management system
$CaCO_3$	calcium carbonate
CEH	Chemical Economics Handbook
CH_4	methane
Cl_2	chlorine
CO	carbon monoxide
Co_3O_4	cobalt oxide
$CoCl_2$	cobalt chloride
DMC	dimethyl carbonate
DOE	U.S. Department of Energy
EC	ethylene carbonate
EPA	U.S. Environmental Protection Agency
GREET	Greenhouse gases, Regulated Emissions, and Energy use in Transportation (model)
H_2O_2	hydrogen peroxide
H_2SO_4	sulfuric acid
HCl	hydrogen chloride
HEV	hybrid electric vehicle
IEA	International Energy Agency
KCl	potassium chloride
LAER	lowest available emission rate
LCA	life-cycle analysis
LFP	lithium iron phosphate
LHV	lower heating value
Li_2CO_3	lithium carbonate
$LiAlSi_2O_6$	spodumene
LIB	lithium ion battery
$LiCoO_2$	lithium cobalt oxide
LiF	lithium fluoride
$LiFePO_4$	lithium iron phosphate

$LiMn_2O_4$	lithium manganese oxide
$LiNiMnCoO_2$	lithium nickel manganese cobalt oxide
LiOH	lithium hydroxide
$LiPF_6$	lithium hexafluorophosphate
MECS	Manufacturing Energy Consumption Survey
$Mg(OH)_2$	magnesium hydroxide
$MgCO_3$	magnesium carbonate
Mn_2O_3	manganese oxide
N_2O	nitrous oxide
Na_2CO_3	soda ash
NaCl	sodium chloride
NAICS	North American industry classification system
NaOH	sodium hydroxide
NCNR	Nevada Department of Conservation and Natural Resources
$Ni(OH)_2$	nickel hydroxide
NMC	lithium nickel manganese cobalt oxide
NMP	N-methyl-2-pyrrolidone
NO_x	nitrogen oxide
OCV	open circuit voltage
PCl_5	phosphorus pentachloride
PE	polyethylene
PET	polyethylene terephthalate
PHEV	plug-in hybrid electric vehicle
PM	particulate matter
PM_{10}	particulate matter with a diameter of 10 micrometers or less
$PM_{2.5}$	particulate matter with a diameter of 2.5 micrometers or less
PP	polypropylene
PVC	polyvinyl chloride
PVDF	polyvinylidene fluoride
RACT	reasonable available control technology
RBLC	RACT/BACT/LAER Clearinghouse
RCCRMARA	Republica de Chile Comision Regional del Medio Ambiente de la Region de Antofagasta
$SCCO_2$	supercritical carbon dioxide
SO_2	sulfur dioxide
SO_x	sulfur oxide
TMS	thermal management system
VOC	volatile organic compound

Units of Measure

Ah	amp hour(s)
µm	micrometer(s)
cm	centimeter(s)
cm^2	square centimeter(s)
cm^3	cubic centimeter(s)
g	gram(s)
kg	kilogram(s)
kWh	kiloWatt hour(s)
L	liter(s)
lb	pound(s)
MJ	megajoule(s)
mm	millimeter(s)
mol	mole(s)
mmBtu	million British thermal units
ppm	part(s) per million
mi	mile(s)
gal	gallon(s)
yr	year(s)
h	hour(s)
hp	horsepower
V	volt(s)

MATERIAL AND ENERGY FLOWS IN THE MATERIAL PRODUCTION, ASSEMBLY, AND END-OF LIFE STAGES OF THE AUTOMOTIVE LITHIUM-ION BATTERY LIFE CYCLE

Jennifer B. Dunn, Matthew Barnes, Linda Gaines,
John Sullivan, and Michael Wang

ABSTRACT

This document contains material and energy flows for lithium-ion batteries with an active cathode material of lithium manganese oxide ($LiMn_2O_4$). These data are incorporated into Argonne National Laboratory's Greenhouse gases, Regulated Emissions, and Energy use in Transportation (GREET) model, replacing previous data for lithium-ion batteries that are based on a nickel/cobalt/manganese (Ni/Co/Mn) cathode chemistry. To identify and determine the mass of lithium-ion battery components, we modeled batteries with $LiMn_2O_4$ as the cathode material using Argonne's Battery Performance and Cost (BatPaC) model for hybrid electric vehicles, plug-in hybrid electric vehicles, and electric vehicles. As input for GREET, we developed new or updated data for the cathode material and the following materials that are included in its supply chain: soda ash, lime, petroleum-derived ethanol, lithium brine, and lithium carbonate. Also as input to GREET, we calculated new emission factors for equipment (kilns, dryers, and calciners) that were not previously included in the model and developed new material and energy flows for the battery electrolyte, binder, and binder solvent. Finally, we revised the data included in GREET for graphite (the anode active material), battery electronics, and battery assembly. For the first time, we incorporated energy and material flows for battery recycling into GREET, considering four battery recycling processes: pyrometallurgical, hydrometallurgical, intermediate physical, and direct physical.

Opportunities for future research include considering alternative battery chemistries and battery packaging. As battery assembly and recycling technologies develop, staying up to date with them will be critical to understanding the energy, materials, and emissions burdens associated with batteries.

1 INTRODUCTION

Hybrid electric vehicles (HEVs), plug-in hybrid electric vehicles (PHEVs), and battery electric vehicles (BEVs) all rely on batteries. To accurately assess the environmental burdens associated with these vehicles (i.e., energy and materials consumption and emissions), researchers must also examine the environmental burdens of the batteries that power them. In this study, we calculate the material and energy flows associated with material production, assembly, and recycling of lithium-ion batteries (LIBs) that use lithium manganese oxide ($LiMn_2O_4$) as the cathode material. Together, material production and battery assembly constitute the cradle-to-gate portion of the overall battery life cycle. The data collected during this study will be incorporated into the vehicle cycle module of the Greenhouse gases, Regulated Emissions, and Energy use in Transportation (GREET) model developed by Argonne National Laboratory (Argonne). Together with the battery use phase data in GREET, these flows culminate in life-cycle energy consumption and air emissions values for LIBs that are rolled into overall vehicle life-cycle impacts and used in life-cycle analyses (LCA) of HEVs, PHEVs, and BEVs.

The purpose of this report is to provide GREET users and LCA practitioners with the data and calculations in GREET that underlie our LIB analysis. In Section 2, we describe our development of a mass inventory of battery components, compiled using Argonne's Battery Performance and Cost (BatPaC) model (Argonne National Laboratory 2011a). In Section 3, we detail the data sources and calculations that underpin the material and energy flows for each battery component and upstream material. Section 4 presents conclusions and plans for future research.

This research has resulted in several improvements in LIB LCA data relative to the data provided in earlier versions of GREET. For example, we now model cathode material production through the pathway shown in Figure 1 (which displays the overall system boundaries for our analysis). Previously, GREET modeled an active material that contained nickel, cobalt, lithium, and manganese. The total energy consumed in producing this material was the sum of the energy required to mine these metals and reduce them to their metallic form, an energy-intensive process. In this new analysis, the metals in the active material are not reduced to their metallic form because this step does not occur in the production of cathode materials. Rather, the cathode material is produced from lithium carbonate (Li_2CO_3) and manganese oxide (Mn_2O_3). Additionally, our analysis now includes transportation impacts for the production of Li_2CO_3 in Nevada and Chile. We have added data for the electrolyte, binder, and binder solvent — components that were previously not included in GREET. Further, we have revised our estimate of the energy intensity of producing the battery management system (BMS). Another improvement is an updated estimate of the energy required to assemble LIBs from their component parts. Finally, we have — for the first time — estimated energy consumption and air emissions for four LIB recycling processes, as discussed in Section 3.10.

In an upcoming journal article, we review recent LCAs of LIBs (Dunn et al. 2012). Here we provide a brief discussion of two recently published LIB LCA papers (Notter et al. 2010; Majeau-Bettez et al. 2011). Both studies used European, rather than U.S., data, and the studies differ significantly in their estimates of the energy consumed during the battery assembly step

(1.3 mmBtu/ton for the assembly step in the Notter et al. study versus 80 mmBtu/ton for the combined battery assembly and all upstream processing in the Majeau-Bettez et al. study). Neither study included an examination of battery recycling processes.

The data in this report can be used to construct an estimate of the energy required to produce LIBs (including materials production and assembly energies) in a United States context and to examine the impacts of battery recycling on that energy estimate. We analyze the energy, materials, and emissions burdens of battery manufacturing and recycling in an upcoming journal article (Dunn et al. 2012).

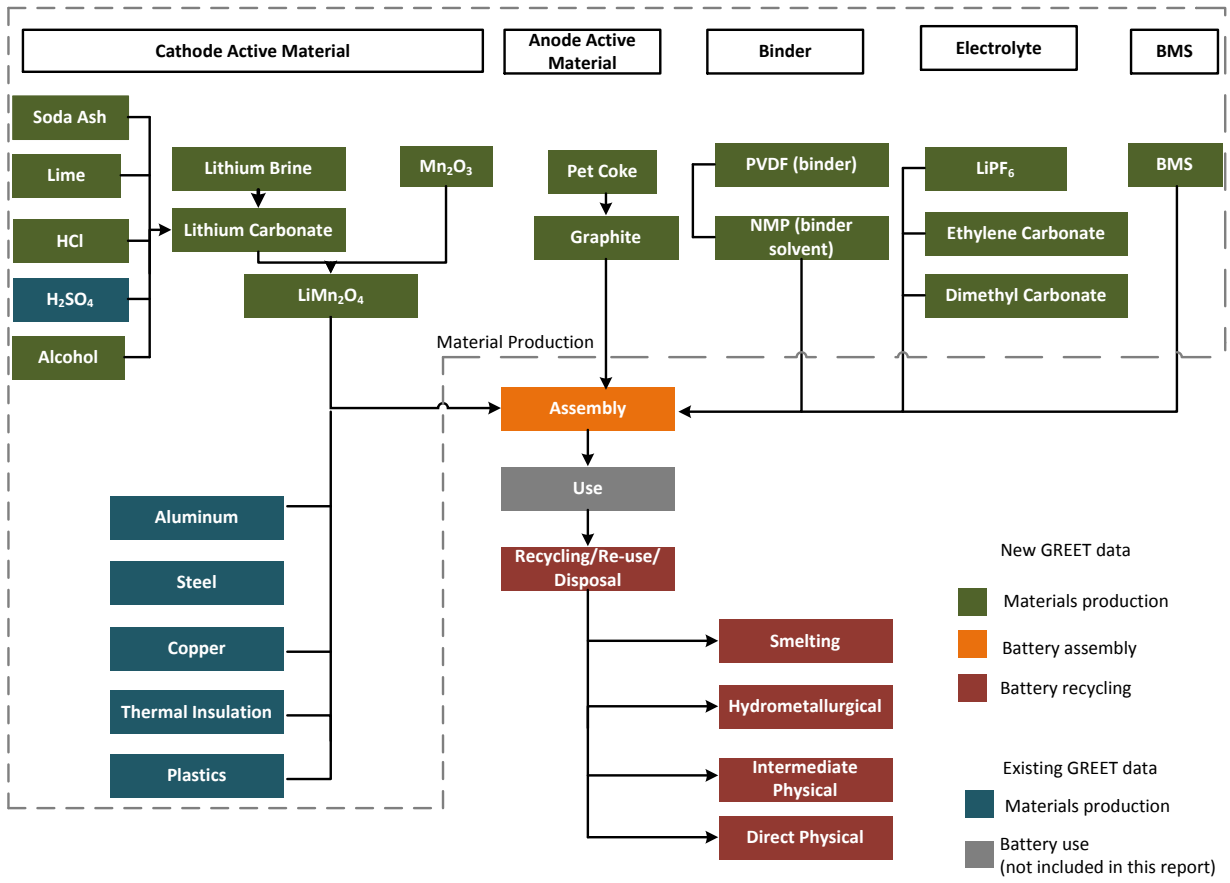


FIGURE 1 Components and Processes with Material and Energy Flows in GREET

2 MATERIAL INVENTORY OF BATTERIES

As diagrammed in Figure 2, two Argonne-developed models (BatPaC and Autonomie) were used to provide inputs to our modeling of automotive battery material and energy flows for GREET.

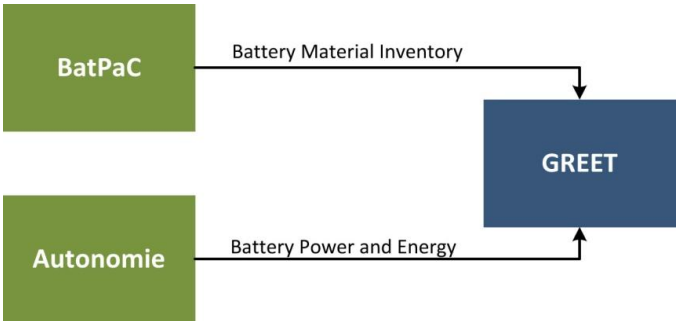


FIGURE 2 Information Flow from Argonne Models into GREET

The first step in our analysis was to use the BatPaC model to develop a mass inventory of battery components. The BatPaC model estimates the manufacturing cost of LIBs in 2020 for incorporation into HEV, PHEV, and BEVs. The model allows users to investigate the effects of different battery designs and material properties on the cost of the battery pack. The model represents present-day technology and manufacturing practices, which it assumes will still be in use in 2020, but allows for some efficiency improvements to yield a more energy-dense battery.

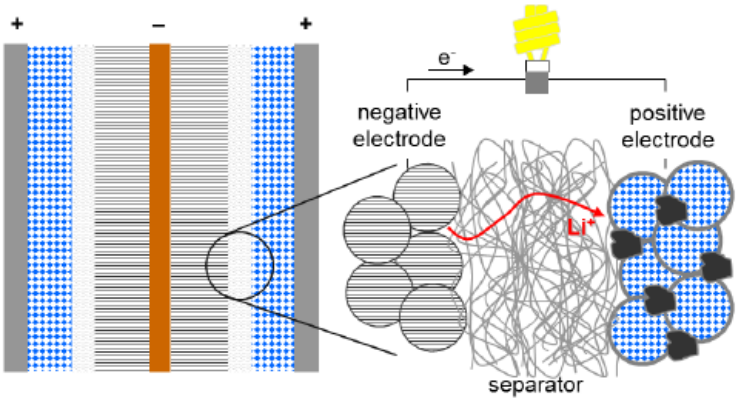


FIGURE 3 Cell Chemistry in a Lithium-Ion Battery (Source: Nelson et al. 2011)

BatPaC adopts a prismatic pouch cell structure, as shown in Figure 3. The pouch is made of a tri-layer polymer/aluminum material (described in detail in Section 2.2). Aluminum and copper foils serve as the current collectors at the cathode and anode, respectively. The anode is coated on both sides with graphite. The cathode material can be one of five chemistries, as described below. A polymeric binder material holds the active material particles together, and a porous membrane separates the two electrodes. The pores of both this separator and the active materials are filled with an electrolyte, modeled in BatPaC as $LiPF_6$ (lithium hexafluorophosphate) in an organic solvent containing linear and cyclic carbonates. During discharge, the lithium ions move from the anode to the cathode while the electrons travel through the current collectors and the external circuit to perform external work. BatPac models these cells as being enclosed in a module (Figure 4); there are six modules per battery.

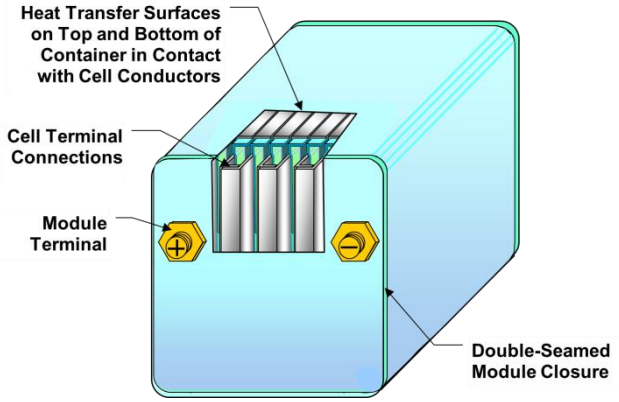


FIGURE 4 Module Structure (Source: Nelson et al. 2011)

BatPaC users can select from among the following five battery chemistries:

1. Lithium nickel cobalt aluminum oxide with a graphite electrode,
2. Lithium nickel manganese cobalt oxide with a graphite electrode,
3. Lithium iron phosphate with a graphite electrode,
4. Lithium manganese spinel with a titanium dioxide electrode, and
5. Lithium manganese oxide spinel with a graphite electrode.

We developed material and energy flows for batteries with $LiMn_2O_4$ as the cathode material; we selected this chemistry because it is one of the most promising, lower-cost alternatives to cobalt-based active materials such as lithium cobalt oxide ($LiCoO_2$) (Okada and Yoshio 2009). Like our study, the Notter et al. (2010) study analyzed a battery that uses $LiMn_2O_4$ as the cathode. Majeau-Bettez et al. (2011), on the other hand, examined different chemistries such as (lithium iron phosphate (LFP) and lithium-nickel-manganese-cobalt-oxide (NMC), reporting similar life-cycle fossil fuel depletion values for each (0.45 and 0.37 kg oil equivalents per storage of 50 MJ, respectively, for NMC and LFP batteries). Their results suggest that differences in cathode materials only minimally influence the life-cycle energy consumption associated with batteries, although in future work, we will investigate this hypothesis by examining additional active materials.

In addition to selecting the active material, users of BatPaC can also specify the battery power, battery capacity, or vehicle range. Battery energy and component masses are dependent on these selections. We modeled batteries as specified in Table 1 on the basis of data from Argonne's Autonomie model (Argonne National Laboratory 2011b) for mid-sized vehicles in 2015. For each battery, we used BatPac parameters of 16 cells per module and 6 modules per battery. Although the batteries were modeled with these characteristics, it is possible to use BatPaC to develop material inventories for batteries with different designs by altering the model inputs (Nelson et al. 2011).

TABLE 1 Battery Parameters

	HEV	PHEV (series)	EV
Power (kW)[a]	30	150	160
Energy (kWh)	2	9	28
Mass (kg)	19	89	210
Specific power (W/kg)	1,500	1,715	762
Specific energy (kWh/kg)	0.10	0.11	0.13
Range (km)	N/A	48	160

[a] Energy storage at peak power (1 second duration).

The following sections describe how the battery component masses were derived from BatPaC results for the three battery types listed in Table 1.

2.1 METALS

This section describes our calculation of the masses of aluminum, copper, and steel in the battery.

Aluminum is used in several places in the battery architecture, including the positive electrode foil, the positive terminal assembly, the cell container, the module wall, the battery jacket, the battery interconnects, the module conductors, and the battery conductors. The mass of foil per cell was calculated by using Equation 1; the result was and multiplied by the number of cells per battery (96).

$$\boldsymbol{M_{Al_foil} = A_{Al_foil} \times \delta_{Al_foil} \times \rho_{Al}} \quad (1)$$

Where M_{Al_foil} = the mass of the aluminum foil (g);
A_{Al_foil} = the area of the aluminum foil (cm^2);
δ_{Al_foil} = the thickness of the aluminum foil (cm); and
ρ_{Al} = the density of aluminum (2.7 g/cm^3).

Three layers comprise the cell pouch: a 30-µm layer of polyethylene terephthalate (PET), a 100-µm aluminum layer, and a 20-µm polypropylene (PP) layer. The cell dimensions change with the battery type and design. The mass of the aluminum layer in the pouch was calculated with Equation 2; the result was multiplied by the number of cells per battery (96). The mass of aluminum in the module wall is a direct BatPaC output.

$$\boldsymbol{M_{C_Al} = \delta_{C_Al} \times L_{cell} \times W_{cell} \times \rho_{Al}} \quad (2)$$

Where M_{C_Al} = the mass of aluminum in the cell pouch (g);
δ_{C_Al} = the thickness of the aluminum layer in the pouch (cm);
L_{cell} = the cell length (cm); and
W_{cell} = the cell width (cm).

The battery jacket, which houses the modules, is also made of a tri-layer material. The outer layers are aluminum, with a thickness of 1.5 mm for the designs examined here. The thickness depends on the number and volume of the modules and can range from one to two mm. The interior layer is lightweight, high-efficiency insulation (10 mm). In GREET, the insulation is modeled as fiberglass. BatPaC calculates the total battery jacket mass, from which we calculate the mass of the aluminum in the jacket with Equation 3.

$$\boldsymbol{M_{J_Al} = \frac{M_J}{\tau} \times \delta_{J_Al} \times \rho_{Al}} \quad 3$$

Where M_{J_Al} = the mass of aluminum in the battery jacket (g);
M_J = the battery jacket mass (g);
τ = the battery jacket weight parameter (g/cm^2); and
δ_{J_Al} = the thickness of the aluminum layers in the jacket (cm).

The jacket weight parameter, τ, is calculated with Equation 4.

$$\boldsymbol{\tau = \delta_{J_ins} \times \rho_{ins} + \delta_{J_Al} \times \rho_{Al}} \quad 4$$

Where δ_{J_ins} = the thickness of the aluminum layer in the jacket (cm); and
ρ_{ins} = the insulation density (0.032 g/cm^3).

Copper is also a major constituent of the battery, used in roles similar to those of aluminum in cell structure and function. The foil of the battery's negative electrode is made from copper. We calculated the mass of foil per cell with Equation 5; the result was multiplied by the number of cells per battery (96).

$$\boldsymbol{M_{Cu_foil} = A_{Cu_foil} \times \delta_{Cu_foil} \times \rho_{Cu}} \quad 5$$

Where M_{Cu_foil} = the mass of the copper foil (g);
A_{Cu_foil} = the area of the copper foil (cm^2);
δ_{Cu_foil} = the copper foil thickness (cm); and
ρ_{Al} = the density of copper (8.92 g/cm^3).

The compression plate and straps are made from steel, the mass of which is a direct BatPaC output.

We did not develop new material and energy flows for the metals in batteries, but instead used wrought aluminum, copper, and steel data from GREET. Burnham et al. (2006) discuss these data and their underlying assumptions.

2.2 ACTIVE MATERIALS, BINDER, AND ELECTROLYTE

The heart of the cell comprises the active materials, the binder that holds them to the positive and negative electrode foils, and the electrolyte. $LiMn_2O_4$ is the active material in the cathode. The mass of the cathode determines the cell capacity and the active material capacity. Carbon black (modeled in our analysis as graphite) is the active material in the anode; it is also present in the positive electrode as a conductor. The two most recent LCA studies of LIBs examine this anode material, which is used in the vast majority of commercial battery cells (Nelson et al. 2011). BatPaC does allow the user to select an alternative anode material, titanate spinel, which we may incorporate into future analyses. The binder, polyvinylidene fluoride (PVDF), holds active material particles together on each electrode.

The electrolyte is $LiPF_6$ in a solution of ethylene carbonate (EC) and dimethyl carbonate (DMC). Nelson et al. (2011) assume a $LiPF_6$ concentration of 1.2 mol/L, and BatPaC calculates a total electrolyte volume per cell. From these parameters, we calculated the mass of $LiPF_6$. We assumed that EC and DMC are present in equal amounts by mass (EMD 2011); we also assumed an average density of 1.2 g/mL. Development of the material and energy flows for the electrolyte components is described in Section 3.6.

2.3 PLASTICS (POLYETHYLENE TEREPHTHALATE, POLYPROPYLENE, AND POLYETHYLENE)

The battery contains three types of plastics: PET, PP, and polyethylene (PE). PET forms the 30-µm-thick outer layer of the pouch; the other 20-µm-thick outer layer is made of PP. The masses of PET and PP in this layer are calculated with Equation 2, substituting the thickness and density of the aluminum layer with that of the individual plastics. The densities of PET and PP are 1.4 g/cm^3 and 0.9 g/cm^3, respectively.

PP is the major constituent of the separator, a porous membrane that measures 20 µm thick and includes a thin PE middle layer. The total mass of the separator was calculated with Equation 6; the result was multiplied by 96 cells per battery. According to Nelson et al. (2011), PP is the dominant separator material, so we assumed PP and PE make up 80% and 20%, respectively, of the total separator mass.

$$\boldsymbol{M_{Sep} = \delta_{Sep} \times A_{Sep} \times \rho_{Sep}} \qquad 6$$

Where M_{Sep} = the mass of the separator (g);
δ_{Sep} = the separator thickness (cm);
A_{Sep} = the separator area (cm^2); and
ρ_{Sep} = the separator density (0.46 g/cm^3) (Argonne National Laboratory 2011a).

GREET contains specific data for PP. For the other plastic components, the data for average plastics can be used. Future updates to GREET will incorporate data specific to PE and PET. Battery calculations will then reference those data, rather than the average plastic data.

2.4 ELECTRONIC PARTS AND TEMPERATURE CONTROL

We consider two types of electronic parts in our inventory. First, each module has a state-of-charge regulator assembly that is composed of circuit boards with insulated wires running to each cell. Second, the BMS includes measurement devices and can control battery pack current and voltage, balance of voltage among modules, and battery thermal management, among other parameters. We develop the mass of the BMS (see Section 3.8) rather than use the BatPaC value for BMS mass, which is calculated as a percentage of total battery mass.

The temperature of a battery is controlled through thermal management and insulation. The battery's thermal management system (TMS) uses a coolant solution made up of a 1:1 ratio (by mass) solution of glycol and water. The total mass of glycol in the TMS is 1,260 g per battery. We do not currently account for TMS mass itself in our analysis. The battery jacket contains an inner layer of insulation that is 10 mm thick. The total mass of this insulation can be calculated with Equation 3, substituting the insulation's thickness and density for that of aluminum. We develop material and energy flows for electronic parts as described in Section 3.8.

2.5 SUMMARY OF MATERIALS INVENTORY

Table 2 lists the mass of each battery component, as determined by BatPaC; cells are approximately 80–90% of the battery mass. Composition is a weak function of battery mass. For the most part, it is reasonable to assume that battery composition is very similar across vehicle types.

TABLE 2 Material Inventories for HEV, PHEV, and BEV Batteries

	Percent Mass		
Component	HEV (%)	PHEV (%)	EV (%)
$LiMn_2O_4$	27	28	33
Graphite/carbon	12	12	15
Binder	2.1	2.1	2.5
Copper	13	15	11
Wrought aluminum	24	23	19
$LiPF_6$	1.5	1.7	1.8
EC	4.4	4.9	5.3
DMC	4.4	4.9	5.3
PP	2.0	2.2	1.7
PE	0.26	0.40	0.29
PET	2.2	1.7	1.2
Steel	2.8	1.9	1.4
Thermal insulation	0.43	0.33	0.34
Glycol	2.3	1.3	1.0
Electronic parts	1.5	0.9	1.1
Total battery mass (lb)	41	196	463

3 MATERIAL AND ENERGY FLOW DATA AND CALCULATIONS

In this section, we describe the data sources and calculations that underpin the new LIB data. Section 3.1 contains these data for lithium brine and Li_2CO_3, which is a raw material for $LiMn_2O_4$ production. The process to make Li_2CO_3 from lithium brine consumes several other compounds for which we have developed new data. The active cathode material we examine here is $LiMn_2O_4$ (Section 3.3), which can be prepared from Li_2CO_3 and manganese oxide (Mn_2O_3) (Section 3.2). Graphite (Section 3.4) is the active material in the anode; the cathode also contains some carbonaceous material. The material and energy flows for the electrolyte components are provided in Section 3.6. Separate sections are devoted to N-methyl-2-pyrrolidone (NMP) (Section 3.7), the BMS (Section 3.8), and battery assembly (Section 3.9). Section 3.10 describes our analysis of four battery recycling processes.

3.1 LITHIUM BRINE AND LITHIUM CARBONATE

Sources of lithium include brine, pegmatites, or sedimentary rocks (Gruber et al. 2011). In the 1970s, spodumene ($LiAlSi_2O_6$) — the most common form of lithium in pegmatite deposits — was the main source of lithium (Kroschwitz and Seidel 2004). Brine is now the most common source, much of it originating from the Salar de Atacama in Chile (Gruber et al. 2011). We have modeled brine from this source and from Nevada (Section 3.1.5) in our analysis. Because essentially all lithium is currently produced from brines, production from ores is not included here. Stamp et al. (2012) discuss ore-based production pathways. Note that five companies produce the lion's share of lithium from brines (Glauser and Inoguchi 2011). We present data for one operation in Chile (SQM) and one in Nevada (Chemetall). Although using such limited data introduces uncertainty into our analysis, this limitation is necessary both because of the confidential nature of the data and the small number of companies engaged in the industry.

Figure 5 depicts a simplified process of producing Li_2CO_3 from lithium brine at the SQM facility in Salar de Atacama, Chile (Kroschwitz and Seidel 2004; Republica de Chile Comision Regional del Medio Ambiente de la Region de Antofagasta [RCCRMARA] 2007). This facility produces the compounds listed in Table 3. Brine, with a lithium concentration of 1,500 ppm, is pumped from wells; the liquid evaporates under controlled conditions in a series of ponds until the lithium concentration is 60,000 ppm (Groves 2011). At the SQM facility, 245,680 gal/yr of diesel fuel is consumed to power electricity generators and brine and water pumps. An additional 824,216 gal/yr is used to fuel equipment that harvests and transports salts (RCCRMARA 2007).

SQM provided top-down production data to Stamp et al. (2012), who allocated energy consumption predominantly to potassium products, arguing that the motivation to run the process is to produce these products. The economic value of the lithium brine, however, is not inconsequential (see Table 3). We therefore allocated the total energy consumption to lithium brine on the basis of the mass fraction of this co-product (0.11). The consumption of diesel fuel is then 0.014 mmBtu/ton of dilute (1,500 ppm) brine based on diesel fuel's lower heating value (LHV). We limit air emissions to combustion emissions and use existing emission factors in GREET (Argonne National Laboratory 2011c) . Concentrated lithium brine is transported to a

processing plant that produces Li_2CO_3. In Chile, the concentrated brine is moved from the Salar de Atacama to the coast at Antofagasta, a distance of approximately 200 mi. The capacity of the trucks carrying the brine is 27 tons (SQM 2001).

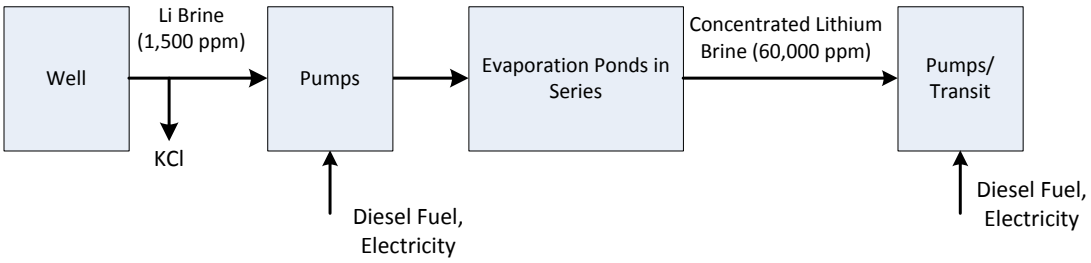


FIGURE 5 Lithium Brine Recovery and Concentration

TABLE 3 Products at SQM Brine Production Facility

Compound	Rate of Production (ton/yr)[a]	Cost ($/ton)	Annual Cost (million $/year)
Potassium chloride	650,000[b]	154[e]	100
Potassium sulfate	250,000[c]	544[e]	136
Boric acid	16,500[c]	827[f]	14
Lithium brine	111,688[d]	1,450[g]	162
Mass fraction lithium brine	0.11	Economic partitioning factor for lithium brine	0.39

[a] Source: RCCRMARA 2007.
[b] Stamp et al. (2012) cites a production rate four times higher, but we used the production rates from the same Chilean documents that were the source of the energy consumption numbers for consistency.
[c] The production rates of potassium sulfate and boric acid are the same in Stamp et al. (2012) and this report.
[d] Stamp et al. (2012) report the Li_2CO_3 production rate, but not lithium brine. Based upon stoichiometry, the lithium brine production rate would be 84,184 tons/year.
[e] Source: Suresh et al. 2010.
[f] Source: Schlag and Kishi 2011.
[g] Source: Glauser and Inogucki 2011. Production cost for Li_2CO_3 in 2009. Production costs for lithium brine are often not public because the brine is commonly used by the producing company to manufacture Li_2CO_3. The annual cost is therefore an upper bound.

Figure 6 illustrates the steps in the production of Li_2CO_3 from concentrated lithium brine (SQM 2001). First, boron is removed from the concentrated brine through addition of hydrogen chloride (HCl), alcohol, an organic solvent, and sulfuric acid (H_2SO_4). Some of the organic solvent can be recycled. In the subsequent first extraction phase, magnesium carbonate ($MgCO_3$) precipitates out of the solution following the addition of soda ash. In the second extraction stage, lime is used to force magnesium hydroxide ($Mg[OH]_2$) and calcium carbonate ($CaCO_3$) out of solution. The purified lithium brine moves to the precipitation reactor, where soda ash (Na_2CO_3) is added to the solution, and Li_2CO_3 precipitates. The resulting solid is washed, filtered, dried, and packaged. The equipment involved in this series of steps includes pumps, centrifuges, filter presses, and material-handling equipment such as bucket elevators (SQM 2001).

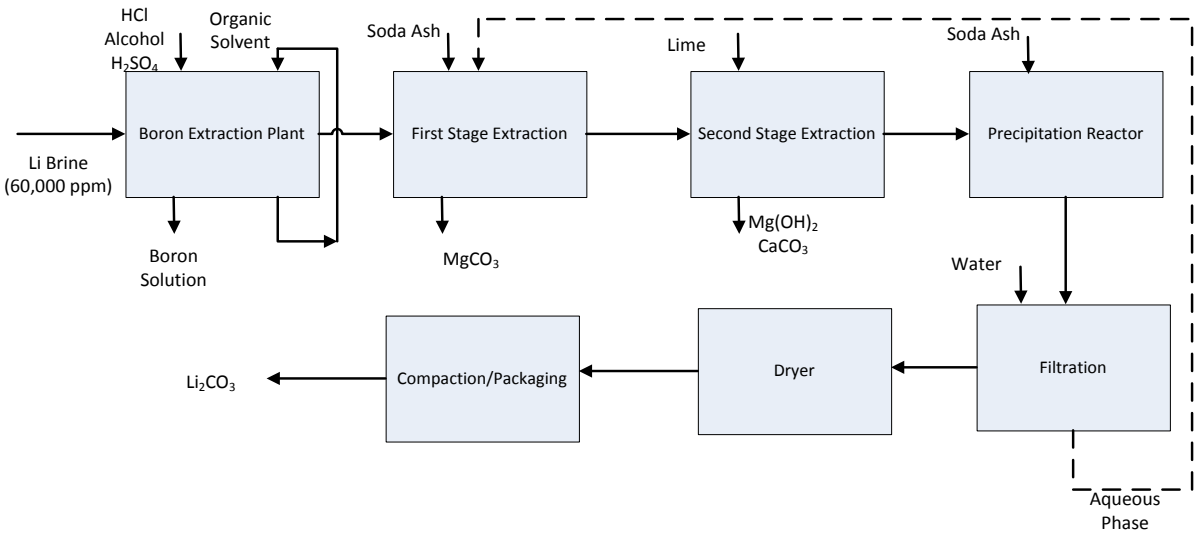


FIGURE 6 Li_2CO_3 Production from Concentrated Lithium Brine (SQM 2001)

Table 4 contains an inventory of the materials consumed during this process, and Table 5 quantifies purchased energy consumption. (Purchased energy intensity is the energy content of the fuel used on-site. If fuel consumption was reported in units of volume, we converted to an energy basis with fuel LHVs in GREET.) Note that for all steps occurring at the SQM facility in Chile, we use the Chilean electricity mix, as presented in Table 6. We assumed that the upstream production processes for the fuels (e.g., natural gas extraction) are similar to U.S. processes. Upstream production impacts are small, and will therefore have a small effect on the energy flows associated with LIB production. Although SQM does make lithium hydroxide (LiOH) as a by-product of Li_2CO_3 production (International Energy Agency [IEA] 2008), no mention is made of a LiOH co-product in the documents we examined; all fuel consumed was for the production of Li_2CO_3. We therefore assigned the full energy consumption and emissions associated with this process to Li_2CO_3.

TABLE 4 Material Consumption (Ton) per Ton Li_2CO_3[a]

Compound	Amount (ton/ton Li_2CO_3)
Concentrated lithium brine (60,000 ppm)[b]	5.45
Soda ash (Na_2CO_3)	2.48
Lime (CaO)	0.09
Hydrochloric acid (HCl)	0.04
Organic solvent	0.02
Sulfuric acid (H_2SO_4)	0.05
Alcohol	7.1×10^{-4}

[a] Sources: SQM 2001; RCCRMARA 2007.
[b] The brine recovery operation processes 40 times this amount of dilute brine, or 218 ton dilute (1,500 ppm) brine per ton Li_2CO_3.

TABLE 5 Purchased Energy Consumption[a]

Energy Source	Amount (mmBtu/ton Li_2CO_3)
Electricity	1.8
Natural gas[b]	2.3
Diesel fuel	6.0

[a] Sources: SQM 2001; RCCRMARA 2007.
[b] The Atacama site documentation is unclear regarding the usage of natural gas versus liquid propane gas (LPG). In 2006, SQM reported that expansion of the Atacama site would result in consumption of 1,440 additional tons/yr of natural gas and that LPG would only be used if natural gas were unavailable (RCCRMARA 2007). Documents describing the 2001 expansion quantify LPG rather than natural gas consumption. For our analysis, we have converted the LPG consumption in the 2001 document to natural gas consumption based upon energy content. We add this figure to the additional natural gas SQM expected to consume after the 2006 expansion.

TABLE 6 Chilean Electricity Mix Used in GREET for Chilean-Based Processes[a]

Source	Percentage of Chilean Grid Power
Coal	24.5
Oil	20
Natural gas	6.5
Biofuels	7.0
Hydropower	41.8
Wind	0.13
Other	0.16

[a] Source: IEA 2012.

In the production of Li_2CO_3, particulate matter (PM) is emitted at a rate of 0.32 kg/h during material handling operations (RCCRMARA 2007). We assumed the only other emissions are from combustion. We also assumed that all the natural gas is consumed in the drying step. The GREET model did not contain emission factors for natural gas combustion in dryers; data for these factors are scarce. As a result, we adopted kiln and calciner volatile organic compound (VOC), carbon monoxide (CO), nitrogen oxide (NO_x), sulfur oxide (SO_x), and PM emission factors from natural gas combustion, as described in Section 3.2. The liquid driven off in this step is water, so no process emissions are assigned to it. Emission factors for electricity generation and diesel combustion are from GREET (Argonne National Laboratory 2011c).

SQM (2001) provides details about the delivery trucks that service the facility. We adjusted these data for increased plant capacity in 2006, assuming the increase in trucks was proportional to the increase in raw materials consumed. Table 7 summarizes the resulting transportation impacts.

In the following sections, we describe the material and energy flow data we gathered for Li_2CO_3 raw materials (Table 4) in our analysis.

TABLE 7 Raw Material and Product Transportation Distances for Li_2CO_3 Production in Chile[a]

Material	Truck Capacity (ton)	Distance Traveled[b]
Brine	27	200 mi
Soda ash (Na_2CO_3)	27	4,433 nautical miles; 850 miles by road[c]
Lime (CaO)	25	20 mi
HCl	24	100 mi
H_2SO_4	28	750[d] mi
Alcohol[d]	25	Brazilian ethanol: 3,900 nautical miles Methanol: 2,000 nautical miles 20 miles by road
Natural gas	7	900 mi by pipeline[e]
Diesel	27	2,000 nautical miles, 20 miles by road[f]
Li_2CO_3	22	800 miles by road; 4,136 nautical miles[g]

[a] Sources: SQM 2001; RCCRMARA 2007.
[b] Based upon information in SQM (2001).
[c] Soda ash comes from the Western United States (Kostick 2001). The nautical distance listed is the distance between the Port of Los Angeles and the Port of Antofagasta, Chile (http://sea-distances.com/). Road distance is from Wyoming to the Port of Los Angeles and from the Port of Antofagasta to the Li_2CO_3 plant.
[d] We assumed H_2SO_4 is a by-product of copper production at the CODELCO El Teniente mine in Machali, Chile.
[e] Ethanol comes from the Port of Paranagua, Brazil, by sea. Methanol comes from Cabo Negro, Chile, by sea.
[f] Natural gas is transported by the Atacama pipeline from Northern Argentina.
[g] Refinery is located in Cabo Negro, Chile. Distribution center is located in Antofagasta.
[h] We assumed the Li_2CO_3 leaves Chile at the Port of Antofagasta and travels to the Port of New York. From there, it travels by truck to a battery plant in Holland, Michigan.

3.1.1 Soda Ash (Na_2CO_3)

The soda ash used in Chilean production of Li_2CO_3 comes from the western United States (see Table 7). It is produced from natural trona deposits (U.S. Department of Energy [DOE] 2002), largely in Wyoming. In the dominant monohydrate process, trona is crushed and undergoes calcination in rotary-gas-fired calciners operating at temperatures between 150°C and 300°C. This process emits carbon dioxide (CO_2) and produces a mixture of 85% soda ash and 15% insolubles. This mixture is dissolved in hot water. Subsequent evaporation in multiple-effective crystallizers yields sodium carbonate monohydrate crystals that precipitate at temperatures between 40°C and 100°C. Some alkali is recovered from the remaining insolubles before the resulting slurry is transported to a tailing pond or injected underground. The crystals undergo further crystallization, then centrifugation. Next, a dehydration process at 150°C produces anhydrous soda ash, which is screened and packaged or stored.

Energy consumption data for this process was obtained from a number of sources. The U.S. Census Bureau's 2007 Economic Census contains limited energy consumption data for North American Industrial Classification System (NAICS) code 212391, which combines potash, soda, and borate mineral mining (U.S. Census Bureau 2007). We divided the energy consumption reported for this NAICS code evenly among these three compounds. This approach likely underestimates the energy consumed during soda ash production; in 2007, soda ash was produced at a rate about nine times that of potash (U.S. Geological Survey [USGS] 2008). The 2007 borate production rate was unavailable. Further, the 2007 Census excluded coal and fuel oil consumption for NAICS code 212291; we obtained these data from the 1997 (coal) and 1992 (fuel oil) Censuses (U.S. Census Bureau 1992, 1997).

Table 8 lists the energy consumption of electricity and each fuel used in the soda ash production process.

TABLE 8 Purchased Energy Consumption during Soda Ash Production[a]

Energy Type	Consumption (mmBtu/ton)	Combustion Process
Coal	4.2	Calcining Kiln
Residual fuel oil	0.4	Residual oil boiler
Distillate oil	1.7×10^{-2}	Diesel oil boiler
Natural gas	3.4×10^{-4}	Calciner
Electricity	8.3×10^{-5}	N/A
Gasoline	1.2×10^{-3}	Stationary reciprocal engine

[a] Sources: DOE 2002; U.S. Census Bureau 2007; USGS 2008.

Soda ash production facilities emit PM during a number of materials handling steps, catalogued in Table 9. Air pollution control devices such as bag filters, cyclones, and electrostatic precipitators limit these emissions. In the production of soda ash, coal is consumed in the calcining and drying steps (DOE 2002). The data from the U.S. Census did not permit differentiation of these two combustion processes, so we attributed all coal consumption to calcining in a kiln. We developed emission factors for coal-fired calcining kilns by using data from the U.S. Environmental Protection Agency's (EPA's) reasonably available control technology (RACT)/ best available control technology (BACT)/lowest available emission rate (LAER) (RBLC) database (EPA 2012) and AP-42 documentation (EPA 1993, 1998). Table 10 lists the emission factors from these sources, from which we chose the best values to use in GREET. VOC emissions from coal-fired kilns are about five times higher than emissions of this pollutant from other coal-fired combustion technologies in GREET but still on the same order of magnitude. On the other hand, SO_x emissions are ten times less than those from coal-fired boiler technologies in GREET. We attribute this result to the built-in SO_x control mechanism in lime kilns in which sodium volatilizing from the Na_2CO_3 entrained in lime mud combines with sulfur dioxide (SO_2) to form sodium sulfate, which is typically captured by the PM control devices on the lime kiln (National Council for Air and Stream Improvement 2009). In addition to CO_2

emissions from fuel combustion, the calcining process releases 127,273 g CO_2/ton Na_2CO_3 stoichiometrically as a reaction product. Nitrous oxide (N_2O) and methane (CH_4) emissions are set at 2.85 g/mmBtu and 0.11 g/mmBtu, respectively (The International Council of Forest and Paper Associations 2005). These values were developed for calciners at kraft mills, but we believe they are representative of emissions from soda ash facility calciners, especially because these emissions are low.

TABLE 9 Non-Combustion Air Emissions from Na_2CO_3 Production[a]

Emissions Source	Filterable PM Emissions (g/ton Na_2CO_3)
Ore mining	1.5
Ore crushing and screening	1.6
Ore transfer	0.10
Soda ash screening	12
Soda ash storage/loading/unloading	2.3
Total	17.5

[a] Source: EPA 1993.

TABLE 10 Combustion Emission Factors for Coal-Fired Kilns[a]

		Emissions (g/mmBtu coal)				
Database ID	Industry	NO_x	PM_{10}	SO_2	VOC	CO
WI-0233	Lime	85	5	29	72	72
WV-0022	Cement				4	374
VA-0272	Cement	0.42		0.41	0.05	0.26
Lime AP-42	Lime		20	40		
Na_2CO_3 AP-42	Na_2CO_3		25			
Best value		40	20	20	10	100

[a] Sources: EPA 1993, 1998, 2012.

3.1.2 Lime

Lime is produced from calcined limestone (EPA 1998). Energy consumption values for limestone mining in the form of delivered cost are from the 2007 U.S. Census Bureau Economic Census for NAICS code 212312 (crushed and broken limestone mining and quarrying) (U.S. Census Bureau 2007). Energy consumption data for lime manufacturing (in the form of delivered cost) are from the Energy Information Administration's (EIA's) Manufacturing Energy Consumption Survey (MECS), which was released in 2009 and contains data for 2006 (EIA 2009). Residual oil and distillate fuel consumption data are from the 1994 MECS (EIA 1997) because the consumption of these fuels in 2006 was below the reporting threshold (the threshold was lower in 1994). To convert fuel consumption from purchased cost to energy content, we used fuel cost data from EIA (www.eia.gov) for the year the fuel was purchased. Production levels for limestone (1.1 billion tons in 2007) and lime (23 million tons in 1994 and 19 million tons in 2006) were obtained from USGS data (USGS 2008; USGS 2010). We assume that 1.875 tons of limestone are processed per ton of lime produced (National Renewable Energy Laboratory 2012). Table 11 lists the energy consumed by type for limestone mining and lime manufacturing.

TABLE 11 Purchased Energy Consumption during Limestone Mining and Lime Production[a]

	Consumption (mmBtu/ton)	
Energy Type	Limestone Mining	Lime Manufacturing
Coal	3.47×10^{-3}	3.38
Diesel	1.23×10^{-2}	0.07
Residual oil	1.55×10^{-3}	0.03
Natural gas	2.00×10^{-6}	0.21
Gasoline	2.43×10^{-3}	0
Electricity	2.44×10^{-4}	0.19

[a] Sources: U.S. Census Bureau 2007; USGS 2008.

Non-combustion emissions during limestone manufacturing include PM_{10} (particulate matter with a diameter of 10 micrometers or less) and $PM_{2.5}$ (particulate matter with a diameter of 10 micrometers or less) emissions from processing and handling of crushed limestone. Table 12 lists controlled PM emissions from these sources.

TABLE 12 Non-Combustion PM Emissions (Controlled) during Limestone Mining[a]

Source	PM_{10} emissions (g/ton)	$PM_{2.5}$ emissions (g/ton)
Tertiary crushing	0.245	0.045
Fines crushing	0.544	0.032
Screening	0.336	0.023
Fines screening	0.998	0
Conveyor transfer point	0.021	0.006
Wet drilling (unfragmented stone)	0.036	0
Truck unloading (fragmented stone)	0.007	0
Truck loading (conveyor, crushed)	0.045	0
Total	2.23	0.106

[a] Source: EPA 1998.

Table 10 lists emissions from the calcining kilns in limestone processing, which are typically coal-fired rotary kilns. In lime processing, CO_2 forms from degradation of $CaCO_3$, yielding 712,537 g CO_2/ton lime based on stoichiometry.

3.1.3 Sulfuric Acid and Hydrochloric Acid

At the SQM facility in Antofagasta, CODELCO, the state-owned Chilean copper mine, is the source of H_2SO_4 (SQM 2001). We therefore assumed that H_2SO_4 is a waste product from a copper mine and attributed no impacts to it other than those associated with transportation.

HCl is manufactured either as a by-product of several processes (e.g., fluorochlorocarbon, perchloroethylene, dichloromethane, trichloroethylene production) or as burner acid (Glauser et al. 2009). When produced as a by-product, most HCl is consumed on-site. Burner acid is mostly manufactured for the merchant market and, at 30% of this market, is the dominant technique used to produce HCl. Burner acid is manufactured at 95–99% purity from "burning" chlorine (Cl_2) gas and hydrogen. Based on stoichiometry, one ton of HCl requires 0.97 ton of chlorine and 0.03 ton of hydrogen (H_2).

Althaus et al. (2007) and Beal and Linak (2011) provide energy consumption data for two processes used to produce Cl_2, one using diaphragm cells and the other using membrane cells. Both processes operate via electrolysis, in which the raw material is saturated sodium chloride (NaCl) brine (25.8 wt% NaCl [Salt Institute 2011]) and the products (in addition to Cl_2) are sodium hydroxide (NaOH) and H_2. The mass share of Cl_2 is 46% (Beal and Linak 2011). In the

United States, the diaphragm cell-based process represents 66% of Cl_2 production (Beal and Linak 2011).

TABLE Table 13 presents energy consumption data from two different data sources, allocated by mass to Cl_2. Both sources consistently predict that the diaphragm process is less energy intensive than the membrane process, and both are reasonably consistent in their reported values for both processes. For each data source, we calculated a weighted average energy consumption for the two process types. In GREET, we adopted the average value of these, or 7.6 mmBtu/ton Cl_2. In addition, the two sources reported that approximately 80% of the energy consumed is electricity and 20% is natural gas. We used these shares in GREET.

TABLE 13 Purchased Energy Consumption during Cl_2 Production

	Diaphragm (mmBtu/ton Cl_2)		Membrane (mmBtu/ton Cl_2)	
Energy Type	Althaus et al. (2007)	Beal and Linak (2011)	Althaus et al. (2007)	Beal and Linak (2011)
Electricity	9.1	4.0	8.6	3.2
Natural Gas[a]	2.3	0.97	0.69	0.49
Total[b]	11.5	5.0	9.3	3.7
Weighted averages[c] (mmBtu/ton Cl_2)				
Althaus et al. (2007)	11		Adopted value	7.6 mmBtu/ton Cl_2
Beal and Linak (2011)	4.6			

[a] Data provided as heat converted to natural gas consumption by dividing by an assumed boiler efficiency of 80%.
[b] Rows may not add directly to total due to rounding.
[c] Assuming 66% and 34% of Cl_2 is produced from the diaphragm cell and membrane cell processes, respectively.

We also considered the energy consumed during production of the NaCl brine. Although NaCl can be mined as rock salt (Boustead 2005a), brine is the dominant form used by the chemical industry (88% in 1996) (Salt Institute 2011). Table 14 contains energy consumption data from two references (Boustead 2005a; Althaus et al. 2007) for production of NaCl brine. We adopted the average value from these two sources for GREET. We also used average values for shares of electricity and natural gas and assumed that residual oil provides the balance of energy, although Althaus et al. (2007) did not include data for this energy carrier.

TABLE 14 Purchased Energy Consumption during NaCl Brine Production

	Althaus et al. (2007) (mmBtu/ton saturated brine)	Boustead (2005[a]) (mmBtu/ ton saturated brine)	Adopted Share Values (%)
Electricity	0.21	0.09	22
Natural Gas	0.36[a]	1.0[b]	67
Residual Oil		0.33	11
Total	0.57	1.46	
Adopted Average Value (mmBtu/ton saturated brine)	1.01		

[a] Data reported as heat and calculated as natural gas consumption by dividing by an assumed boiler efficiency of 80%.

[b] Boustead (2005[a]) report natural gas in a category called "other fuels." From this aggregate value, we subtracted the recovered energy and assumed delivered energy from coal and other minor energy carriers in this process to be provided by natural gas.

To determine the energy burden that Cl_2 production incurs from consuming NaCl brine, we multiply the energy intensity of producing the brine by the consumption rate of brine in Cl_2 production. Althaus et al. (2007) state that 1.8 tons of dry NaCl is consumed per ton of Cl_2. Boustead (2005[a]) sets this ratio at 0.92 ton of dry NaCl per ton of Cl_2. (Note that these ratios reflect allocation of total NaCl brine consumption to Cl_2 production.) We converted both of these ratios to reflect the mass of saturated brine (28.5 wt% NaCl) that the Cl_2 processes consume and calculated the average. The resulting value, which we used in GREET, is 5.17 tons of saturated brine per ton of Cl_2.

We adopted GREET data for H_2 production (central plants) (Argonne National Laboratory 2011c) and used a stoichiometric H_2 intensity of 0.03 ton H_2 per ton of HCl. The reaction between H_2 and Cl_2 to produce HCl is very exothermic (Althaus et al. 2007) and may require no thermal energy. We therefore include no energy consumption for the actual production of HCl.

3.1.4 Alcohol

We assumed that the alcohol used at Antofagasta is either ethanol from Brazil or methanol from a refinery in Southern Chile. We use GREET model data for both options.

3.1.5 Lithium Carbonate Production in Nevada

Although Chile is the primary source of Li_2CO_3, this compound is also produced in Nevada. The lithium brine in Nevada, however, is about seven times less concentrated than Chilean brine (Gruber et al. 2011), requiring the processing of more brine to yield the same amount of Li_2CO_3. The primary data source for Li_2CO_3 produced in Nevada is an operating permit from the Nevada

Department of Conservation and Natural Resources (NCNR) to Chemetall Foote Corporation (NCNR 2010). This facility, located in Silver Peak, Nevada, recovers lithium brine, concentrates it, and converts it to Li_2CO_3 at a permitted rate of 7,000 tons/yr. The site also produces 2,000 tons/yr of anhydrous LiOH. Garrett (2004) is another source of information for Nevada-based production of Li_2CO_3.

The facility in Nevada consumes residual oil in two boilers and propane in a dryer (NCNR 2010). Although the permit states that the facility operates nine pieces of gasoline-powered equipment (e.g., pumps, welders, pipe-fusers) and four pieces of diesel-powered equipment (e.g., well drillers, dredgers, pumps, welders), it does not limit or estimate the amount of gasoline and diesel consumed. We therefore use information from Garrett (2004) concerning the vehicle population (12 dump trucks, five bottom dumps, and one yard loader) to estimate equipment diesel consumption. A staff of nine operates the fleet (Garrett 2004). We estimated that eight pieces of equipment operate 20 h/week for 50 weeks/yr to calculate the total annual fleet hours of operation (8,000). We further assumed each vehicle is 300 hp and calculated an average annual fuel consumption of 38,000 gal. Further, we assumed the site operates a 500-hp salt harvester that operates 5,600 h/yr and consumes 132,000 gal of diesel fuel to remove salt that has accumulated in the evaporation ponds. Finally, we developed an estimate of the total power required for pumping on the basis of information in Garrett (2004). We assumed that the pumps operate 5,760 h/yr.

Table 15 lists the energy and materials consumed during production of Li_2CO_3 in Nevada. Note that the total energy consumption at the site is allocated between LiOH and $Li2_2CO_3$ on a mass-production basis. The resulting purchased energy intensity for Li_2CO_3 in Nevada is three times greater than our estimated energy intensity for Chilean-based production. One key difference between the sites is that brine in Nevada is seven times less concentrated than lithium brine in Chile. In addition, the Nevada site operates two residual-oil fueled boilers. Documentation for the Chilean site does not mention a boiler but does provide total fuel consumption, as reported in Section 3.1.

TABLE 15 Purchased Energy Consumption during Li_2CO_3 Production in Nevada[a]

Equipment	Energy Consumption (mmBtu/ton Li_2CO_3)	Fuel
Two boilers	25	Residual oil
Dryer	1.5	Propane
Pumps	1.9	Off-Road Diesel
Mobile equipment	2.6	Off-Road Diesel
Total	31	

[a] Sources: Garrett 2004; NCNR 2010.

Equipment at the Nevada Li_2CO_3 production facility (e.g., conveyor belts, shakers, screens) likely consumes electricity, but the lack of data about such equipment precludes our estimation of electricity consumption at the site. The reported lime consumption rate is nearly 30 times higher than that at the Chilean facility.

From the NCNR permit, we determined that, for each ton of Li_2CO_3 produced, 2.5 and 3.0 tons of lime and soda ash, respectively, are consumed.

Stationary source emissions from the facility are provided in Table 16. These are not-to-exceed, worst-case-scenario emissions (NCNR 2010). We do not include PM_{10} emissions from the material handling of co-product LiOH.

TABLE 16 Emissions from Li_2CO_3 Production in Nevada

Pollutant		Emissions (g/ton Li_2CO_3)
Material Handling: PM_{10}[a]		160
Combustion[b]:	PM_{10}	2.1
	SO_2	0.8
	NO_x	115
	CO	19
	VOC	2.4

[a] Emissions from material handling operations including pond liming, soda ash conveying, lithium carbonate lime system, transfer conveyer, warehouse bin, milled Li_2CO_3 air classifier system, Li_2CO_3 handling, lime handling.

[b] Combustion in the propane-fired rotary dryer. Other fossil fuel combustion emissions are calculated in GREET from the fuel throughput.

Presumably, the Li_2CO_3 produced in Nevada would be transported to a facility that produces $LiMn_2O_4$. For the present, we assumed that this facility would be located near the battery assembly plant, which we assume to be in Holland, Michigan. The Li_2CO_3 travels 2,800 miles by rail and 200 miles by truck to reach this destination.

3.2 MANGANESE OXIDE

In addition to Li_2CO_3, manganese oxide (Mn_2O_3) is one possible raw material for $LiMn_2O_4$ production. Manganese can also be in the form of a salt (Singhal and Ganesh 2005) or Mn_3O_4 (Han et al. 2003). Mn_2O_3 is made by heating manganese ore in a kiln operating at temperatures between 500°C and 800°C (Kroschwitz and Seidel 2004). We developed an estimate for the energy consumed during this step by using data from industrial processes (Brown et al. 1996). Figure 7 shows the data for three processes that employ kilns. We developed a best estimate for energy consumption by the kiln during the Mn_2O_3 production process of 2.5 mmBtu/ton at 800°C on the basis of these data.

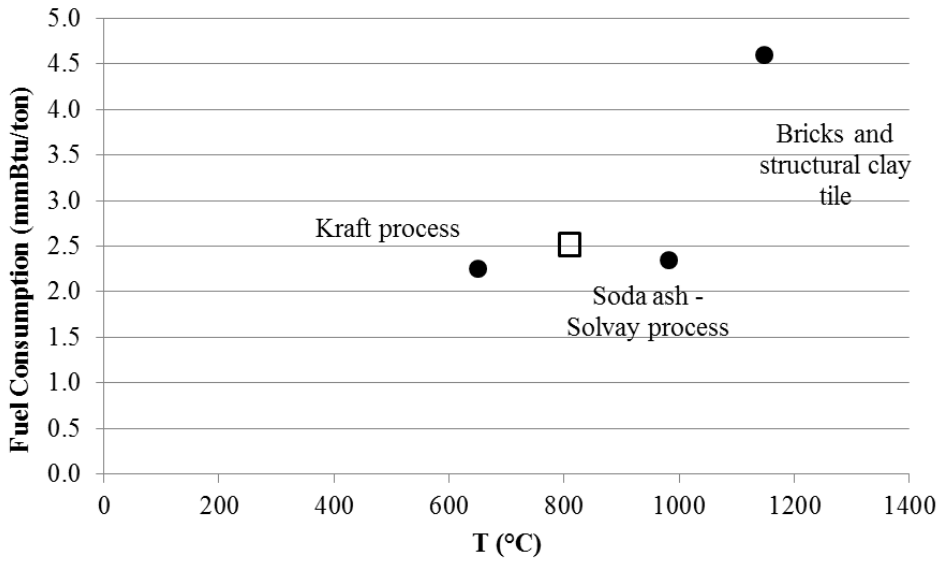


FIGURE 7 Energy Intensity of Industrial Kilns in Three Processes (Source: Brown et al. 1996)

Kilns also consume electricity. Averaging the kiln energy consumption for the brick and soda ash processes yields 0.07 mmBtu/ton electricity consumption. (Brown et al. [1996] did not provide an electricity consumption value for the kiln in the Kraft process.)

We calculated process CO_2 emissions during Mn_2O_3 production from the stoichiometry in Equation 7; the resulting value is 505,800 g CO_2/ton Mn_2O_3. We developed emission factors for VOC, CO, NO_x, and SO_x emissions from kilns by analyzing data in EPA's RBLC database and obtaining permitted emission limits for six natural-gas fired lime kilns (EPA 2012). From these data, summarized in Table 17, we selected the best values for gas-fired kiln emission factors. Note that the emission factors based on data from the EPA database are likely higher than those from AP-42 documentation because facilities tend to choose worst-case emission levels that they will probably not exceed, thereby avoiding fines. With the exception of VOC, CO, and NO_x emission factors for stationary reciprocating engines, the emission factors in Table 17 are higher than emission factors in GREET for other natural-gas fired technologies. This trend may be explained by the nature of emissions rates reported in the RBLC database, as described above. For PM_{10}, the higher emission factors may be explained by the dustier nature of a process for handling solids. The values we chose for this analysis are therefore conservative.

$$2MnCO_3 + {}^1\!/_2\, O_2 \rightarrow 2CO_2 + Mn_2O_3 + H_2O \qquad 7$$

TABLE 17 Emission Factors for Gas-Fired Kilns[a]

	Emissions (g/mmBtu natural gas)				
Database ID	NO_x	PM_{10}	SO_2	VOC	CO
AL-0245	66				
MS-0077	300	93	73		
OR-0044	116				
MS-0075	217	48	28		27
LA-0122	332	125	27	27	6
OH-0321	3,490	196	1,447	204	1,073
Lime AP-42	18	2	0.09		34
Best value	100	90	30	100	50

[a] Sources: Research Triangle Institute 2000; EPA 2012.

CO_2 emissions are calculated as the total carbon present in the fuel source minus the carbon in emitted VOCs, CO, and CH_4. We adopted CH_4 and N_2O emission factors of 2.85 g/mmBtu and 0.11 g/mmBtu, respectively, for natural gas-fired kilns (The International Council of Forest and Paper Associations 2005).

We assumed that the Mn_2O_3 would travel 500 miles by truck to reach the facility that prepares $LiMn_2O_4$.

3.3 LITHIUM MANGANESE OXIDE

$LiMn_2O_4$ is produced by means of the process illustrated in Figure 8.

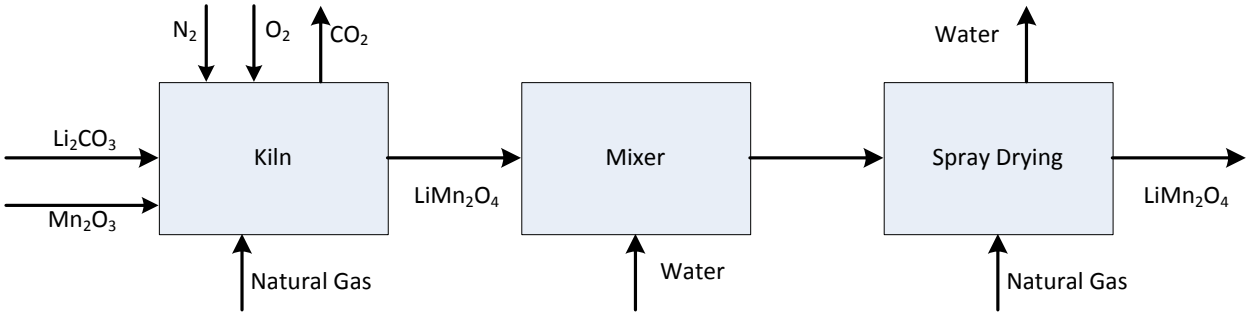


FIGURE 8 Production of $LiMn_2O_4$

For $LiMn_2O_4$ production, we adopted values from the literature (Notter et al. 2010). For each ton of $LiMn_2O_4$ produced, 0.02 mmBtu and 13 mmBtu of electricity and process heat are consumed, respectively. We assumed that the process heat derives from natural gas, which is combusted in a kiln. The natural gas consumption accounts for the kiln's efficiency, although Notter et al. (2010) do not specify this efficiency. (Kiln emission factors are as described in Section 3.2.) Further, we used stoichiometry (1 mol CO_2 per 2 mol $LiMn_2O_4$) to calculate process CO_2 emissions of 110,400 g CO_2/ton $LiMn_2O_4$.

We assumed that $LiMn_2O_4$ is produced within 20 miles of the battery assembly plant that will use it.

3.4 GRAPHITE

The production of graphite from calcined coke includes two high-temperature steps: baking (800°C–1,000°C) and graphitization (3,000°C) (Kroschwitz and Seidel 2004). The aluminum industry uses graphite electrodes for the electrolysis of alumina in the Hall–Héroult process (Kroschwitz and Seidel 2004). In our examination, the graphite electrodes used in aluminum production are assumed to be comparable to the graphite anodes used in Li-ion batteries. Other analysts used the same assumption when assessing the impacts of graphite (Majeau-Bettez et al. 2011). Aluminum production has been the focus of several LCAs (International Aluminum Institute 2007; European Aluminum Association 2008; PE Americas 2010). In our study, we incorporate U.S. data from the Aluminum Association (PE Americas 2010), listed in Table 18.

Further, 0.79 tons of petroleum coke and 0.21 tons of hard pitch are required to produce one ton of graphite (PE Americas 2010). For both these raw materials, we used the energy and emissions impacts of petroleum coke, as calculated in GREET (Argonne National Laboratory 2011c).

TABLE 18 Purchased Energy Consumption during Graphite Production[a]

Energy Carrier	Amount Consumed (mmBtu/ton)
Electricity	0.42
Natural gas	2.04
Residual oil	0.18
Coal	0.09
Total	2.7

[a] Source: PE Americas 2010.

TABLE 19 Purchased Energy Consumption during PVDF Production[a]

Energy Carrier	Amount Consumed (mmBtu/ton)
Electricity	8.4
Residual oil	0.79
Natural gas	12

[a] Source: Ostermayer and Giegrich 2006a,b.

3.5 POLYVINYLIDENE FLUORIDE

PVDF is used in LIBs to bind together the electrode materials. Energy and emissions data for PVDF were not available. We therefore adopted the energy intensity of polyvinyl chloride (PVC) production for that of PVDF. Our study used an average of energy requirements for cradle-to-gate production of suspension and emulsion polymerization PVC from the PlasticsEurope

database (Ostermayer and Giegrich 2006a,b). Table 19 summarizes the adopted energy intensity values used for this battery component.

3.6 ELECTROLYTE

$LiPF_6$ is the electrolyte for many LIBs, yet few analyses have been conducted to determine its environmental burdens. The most relevant information about the energy and emissions burdens of this material was obtained from an LCA of product integrated polymer solar cells using lithium-polymer batteries (Espinosa et al. 2011). The energy intensity for $LiPF_6$ production in this reference is based upon first principles, although the methodology was not described in detail. Table 20 provides purchased energy consumption during $LiPF_6$ production. The production of $LiPF_6$ precursors, lithium fluoride (LiF) and phosphorus pentachloride (PCl_5), was not considered.

TABLE 20 Purchased Energy Consumption during $LiPF_6$ Production[a]

Energy carrier	Amount Consumed (mmBtu/ton)
Electricity	73
Fuel oil	0.4

[a] Source: Espinosa et al. 2011.

$LiPF_6$ is mixed with EC and DMC to increase permittivity. DMC can be made from EC, which in turn, is made from ethylene oxide. The feedstock for ethylene oxide production is ethylene. Material and energy flow data for these materials are compiled from data for individual production steps, beginning with a cradle-to-gate assessment of ethylene (Boustead 2005b). We included the energy embodied in the natural gas and petroleum inputs to ethylene production (National Renewable Energy Laboratory 2012). Process CO_2 emissions generated during the production of ethylene are 154,224 g CO_2/ton ethylene (Boustead 2005b). Table 21 provides purchased energy consumption during ethylene production.

Data for energy and materials consumed during the production of ethylene oxide from ethylene were obtained from the U.S. LCI Database (National Renewable Energy Laboratory 2012). Table 22 contains these data.

TABLE 21 Purchased Energy and Feedstock Consumption during the Production of Ethylene[a]

Energy Carrier or Feedstock	Amount Consumed (mmBtu/ton)
Electricity	0.56
Natural gas	3.2
Residual oil	7.7
Natural gas (feedstock)	34
Petroleum (feedstock)	87

[a] Sources: Boustead 2005b; National Renewable Energy Laboratory 2012.

TABLE 22 Purchased Energy and Materials Consumed during the Production of Ethylene Oxide[a]

Energy Carrier or Feedstock	Amount Consumed
Electricity (mmBtu/ton)	0.69
Natural gas (mmBtu/ton)	3.18
Ethylene (ton/ton ethylene oxide)	0.79

[a] Source: National Renewable Energy Laboratory 2012.

Energy consumption during production of DMC from ethylene oxide was obtained from a study that compared several processes that use sequestered CO_2 in the production of DMC (Monteiro et al. 2009). We chose the scenario in which CO_2 and ethylene oxide react in plug flow reactors. Subsequently, the EC that is produced reacts with methanol in a second plug flow reactor to yield DMC and ethylene glycol. Monteiro et al. (2009) provide a net total energy for this process that includes 79% recovery of net heat possessed. From this net total energy, we subtracted the electricity required to power the pumps and assumed the remainder is thermal heat provided by natural gas. We allocate the energy burden of this process between DMC and ethylene glycol by mass.

Table 23 contains the parameters in our analysis for DMC that derive from Monteiro et al. (2009).

TABLE 23 Parameters for the Production of DMC[a]

Parameter	Value
Net energy use (mmBtu/ton DMC)	1.4
Total electricity consumption (mmBtu/ton DMC)	0.087
Natural gas consumption (mmBtu/ton DMC)	1.27
Production rate of DMC (kg/h)	2,080
Production rate of ethylene glycol (kg/h)	9,296
Energy consumption allocated to DMC (%)	18
Feed rate of ethylene oxide (ton/ton DMC)	0.58

[a] Source: Monteiro et al. 2009.

It is possible to isolate EC after the first step of this process. We summed the energy consumption for the steps that lead up to the production of EC to develop an estimate of the energy intensity of EC production (Table 24).

TABLE 24 Purchased Energy and Materials Consumed during the Production of EC

Parameter	Value
Electricity (mmBtu/ton)	0.04
Natural gas (mmBtu/ton)	0.22
Ethylene oxide (ton/ton EC)	0.16

[a] Source: Monteiro et al. 2009

3.7 N-METHYL-2-PYRROLIDONE

NMP is used as a solvent during the battery manufacturing process, although none remains in the final battery. About 99.5% of the NMP is recovered and can be reused, but the balance is combusted and must be replaced (Nelson et al. 2011). BatPaC provides the amount of NMP and active material the battery manufacturing process consumes. The ratio of the two is 0.007 ton NMP/ton $LiMn_2O_4$. Energy consumption data for the production of NMP is provided in Table 25 (Sutter 2007). We did not include the burdens associated with producing the raw materials for NMP production (butyrolactone and methyl amine) because the LIB consumes little NMP.

3.8 BATTERY MANAGEMENT SYSTEM

The BMS is the collection of electronic components (e.g., semiconductors, circuit boards, sensors) that measure and monitor cell voltage, temperature, and current and perform basic battery functions such as cell balancing and ensuring battery longevity and safety. Semiconductor manufacturing involves highly controlled metal deposition and chemical etching processes.

TABLE 25 Purchased Energy Consumption during the Production of NMP

Energy Carrier	Amount Consumed (mmBtu/ton)
Natural gas	1.72
Electricity	1.03

[a] Source: Sutter 2007.

In the literature, assessments of BMS contribution to overall battery life-cycle impacts typically approximate BMS mass as a percentage of battery mass (Majeau-Bettez et al. 2011; Nelson et al. 2011). To develop a more robust estimate of BMS impacts, we obtained a battery pack from Argonne's Advanced Powertrain Research Facility. We measured the physical parameters of this module and a circuit board for a BEV (Table 26). Although the cathode material of the obtained battery pack is lithium iron phosphate ($LiFePO_4$), we used this pack's parameters because we did not have access to the BMS from a battery with $LiMn_2O_4$ cathode material. The type of active material is not expected to greatly influence BMS impacts on battery life-cycle energy consumption and emissions. For example, Majeau-Bettez et al. (2011) do not report a significant difference in the BMS impact on fossil fuel depletion for LFP and NMC-based LIBs.

TABLE 26 Measurements of a Battery Pack

Parameter	Measured Value
Energy (kWh)	5
Control unit area (cm^2)	323
Sensor area (cm^2)	542
Total BMS semiconductor area (cm^2)	865
Circuit board (BEV) BMS area (cm^2)	42.74
Circuit board (BEV) BMS mass (g)	19
Area density (g/cm^2)	0.45

To develop material and energy flows for BMS production, we calculated areas for two separate pieces of the BMS that involve different energy intensities for manufacture: circuit boards and semiconductors.

First, we assumed that the area of a BMS circuit board scales with battery energy; we used Equation 8 to calculate the circuit board area in the modeled battery's BMS:

$$\boldsymbol{A_1 = \frac{E_1}{E_2} A_2} \qquad 8$$

Where A_1 is the area of the circuit boards (cm^2) in the modeled battery;
E_1 is the energy of the modeled battery (kWh) (average of values in Table 1);
E_2 is the energy of the sample battery (5 kWh);
and A_2 is the area of circuit boards in the sample battery (54 cm^2).

We also assumed that the semiconductor area scales linearly with the circuit board area. To obtain the relationship between these two parameters, we use the ratio between semiconductor area and circuit board area for desktop computers (Yao et al. 2010), as shown in Table 27.

TABLE 27 Desktop Computer Circuit Board and Semiconductor Areas[a]

Parameter	Value
Desktop computer semiconductor area for a 2009 system (cm^2)	7
Desktop printed circuit board area for a 2009 system (cm^2)	0.07
Desktop semiconductor area per circuit board area (cm^2/ cm^2)	0.01

[a] Source: Yao et al. 2010)

We determined the mass of the BMS by multiplying the area of the circuit board in the BMS by the area density in Table 26.

Next, we adopted energy intensity factors for the production of circuit boards and semiconductors from Deng et al. (2004), shown in Table 28, to calculate the energy to produce a given BMS mass. These factors were developed for desktop computers, but we assume they are sufficiently representative of the energy intensity of vehicle battery circuitry production in the absence of any more specific data.

TABLE 28 Energy Intensity of Circuit Board and Semiconductor Production[a]

		Value	
Fuel	Component	MJ/cm^2	mmBtu/ton
Natural Gas	Circuit Board	0.01	22
	Semiconductor	3.2	62
	Total	2.7	84
Electricity	Circuit Board	0.003	22
	Semiconductor	1.5	99
	Total	1.5	121

[a] Source: Deng et al. 2011).

3.9 BATTERY ASSEMBLY

It has proven difficult to collect energy consumption data from battery assembly plants for several reasons. First, most battery assembly takes place overseas. Second, of the battery manufacturers in the United States, many are just beginning manufacturing, and some are still building manufacturing facilities and therefore have not yet collected production-representative data. The third, and perhaps most challenging reason, is that companies regard energy consumption data during production as proprietary and are reluctant to share it.

Without facility-level data in hand, we were required to estimate the energy intensity of the battery manufacturing step. In examining the battery assembly process, as described in Nelson et al. (2011) and diagrammed in Figure 9, we found that the process consists of mechanical, electricity-driven steps. We identified the dry room step as a major energy consumer. At our request, a dry room manufacturer — SCS Systems (Mitchell 2011) — provided a quote for a dry room (1,860 m^2) with the following characteristics. Two dehumidification systems maintain a relative humidity of 0.5% at 21°C. The systems incorporate a desiccant wheel with indirect-fired natural gas reactivation, electric heating, and electric motors. We assume that energy consumption scales linearly with the dry room area and adjust the energy consumption to correspond to the dry room area in BatPaC (3,000 m^2). SCS Systems provided electricity and natural gas consumption on an annual basis. We converted those values to a per-mass-of-battery basis for incorporation into GREET using the average mass of the batteries listed in Table 1 and a cell production rate of six million accepted cells per year (Argonne National Laboratory 2011a). The dry room consumes 0.60 mmBtu/ton battery of electricity and 1.1 mmBtu/ton battery of natural gas.

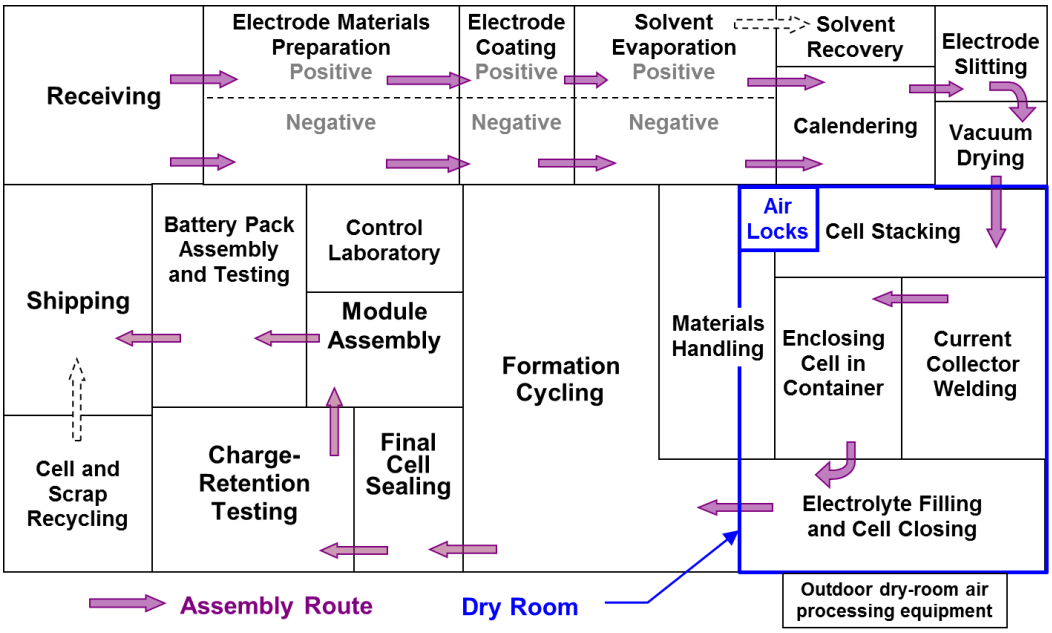


FIGURE 9 Battery Manufacturing Plant Schematic (Source: Nelson et al. 2011)

The formation cycling step is potentially another major energy consumer. Lithium-ion cells are assembled in a discharged state and undergo this step to activate them (Tagawa and Brodd 2009). The first, formation charge activates the active materials and creates the solid electrolyte interphase on the anode. The cell voltage is measured after the first charge, and the battery is left to age for a manufacturer-specific time. Measuring the change in cell voltage before and after formation cycling identifies underperforming cells that can be discarded. The number of cycles that cells undergo after the first formation cycle depends on the manufacturer , but it typically would not exceed two additional cycles (Tagawa and Brodd 2009). We calculated the energy associated with formation cycling with Equations 9–11.

$$E_{C1} = \frac{C \times OCV_{avg}}{\eta_{C1} \times \eta_{Cell}} \quad (9)$$

Where E_{C1} is the energy for the first charge cycle;
C is the cell capacity (Ah);
OCV_{avg} is the average cell open circuit voltage (V);
η_{C1} is the first cycle coulombic efficiency; and
η_{Cell} is the cell efficiency.

$$E_{C2} = C \times OCV_{avg} \times \eta_{Cell} \quad (10)$$

Where E_{C2} is the energy for the second charge cycle.

$$E_{D} = C \times OCV_{avg} \times \eta_{Cell} \quad (11)$$

Where E_D is the energy for the battery discharge.

Values for C and OCV_{avg} are dependent upon cell chemistry and were determined from BatPaC. Average C and OCV_{avg} values for the batteries in Table 1 are 29.5 Ah and 3.9 V, respectively. We used values of 0.98 and 0.87 for η_{Cell} and η_{C1}, respectively (Gallagher 2011) and assumed one formation cycle and three additional cycles, which results in an energy intensity for this step of 0.034 mmBtu/ ton battery, or for the average of energies in Table 1, 370 Btu/kWh battery capacity. For our analysis, we estimated that the dry room and cycling steps represent 60% of the electricity consumed at the manufacturing facility (Moneypenney 2011). The resulting energy consumption for battery assembly is 2.3 mmBtu/ton battery. This value is very close to that reported by Notter et al. (2010).

3.10 RECYCLING PROCESSES

In this report, we describe material and energy flows for four recycling processes that target different battery chemistries, including those that we have not yet examined: hydrometallurgical, pyrometallurgical, and intermediate and direct physical processes. We use the term "intermediate" to indicate that cathodic active material can be obtained from upgrading of process outputs. We use the term "direct" to indicate that process outputs can be reincorporated into batteries with little or no additional processing. It is important to emphasize that the technologies described in the following sections are at different stages of development. The hydrometallurgical and direct physical recycling processes are under development, whereas the pyrometallurgical and intermediate physical recycling processes are commercial.

All four processes were largely developed to recover cobalt, rather than lithium, because cobalt is a higher-value metal. However, vehicle battery chemistries are moving away from cobalt because of cost, scarcity, and safety issues, leaving recycling technologies behind the progression of battery technology itself. For example, the pyrometallurgical process can recover cobalt and nickel from LIBs with a cobalt- and nickel-containing active material, but the process cannot recover the lithium itself. The hydrometallurgical and intermediate and direct physical recycling processes can recover lithium-containing materials, but these materials must undergo further processing to regenerate useable active material. None of these processes was specifically designed to handle batteries with $LiMn_2O_4$ chemistry. In our upcoming paper [Dunn et al. 2012], we assume that these technologies could be used to recycle batteries with $LiMn_2O_4$ cathodes and examine the role they might play in reducing energy and emissions associated with battery material production and assembly. As we expand GREET to include cathode materials containing cobalt, we will reexamine these recycling processes in the context of cobalt-containing active materials.

Two fates are possible for the materials recovered from recycling processes. In an open-loop recycling scenario, they would be available to the greater economy for incorporation into any product. In a closed-loop recycling scenario, these materials would be reincorporated directly into batteries. For this study, we consider the second option. Preliminary analyses indicate that recycling the lithium, aluminum, and copper using one of the three technologies that we assumed could recover these compounds (hydrometallurgical and intermediate and direct physical

recycling) could reduce the energy intensity of the batteries examined in this study by up to approximately 40% to 50%. The bulk of this reduction would result from the recycled aluminum when energies for melting and casting, sheet production and rolling, and stamping of the recovered aluminum are included.

Given the changing battery chemistries on the market and the immaturity of recycling technologies, advances in automotive battery recycling technologies are likely. We developed material and energy flows for the processes described in this section to enable an analysis of the effect of a number of different recycling techniques on the overall environmental burdens associated with batteries. We will stay up to date on battery recycling technologies and will update material and energy flow data in GREET accordingly.

3.10.1 Hydrometallurgical Recycling Process

Hydrometallurgical processing is one technique used to recover the metals in a battery's active materials (both cathode and anode). Figure 10 depicts one such process, which is under development (Li et al. 2012) and has been applied to spent laptop batteries with $LiCoO_2$ cathode chemistry. We applied it to spent vehicle batteries with $LiMn_2O_4$ cathodes and assumed that the same cobalt and lithium recovery rates are achieved for vehicle and laptop battery cells under the same conditions. We do not address the fate of manganese in this analysis because experiments did not assess its behavior in this process. We used vehicle battery composition data from BatPaC as described in Section 2.

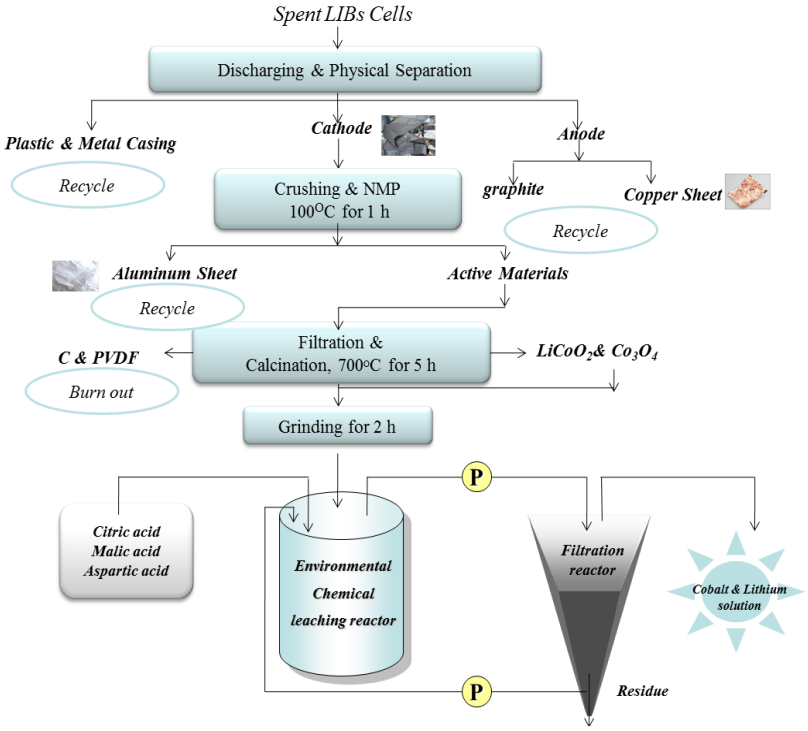


FIGURE 10 Flow Sheet of Hydrometallurgical Recycling Process

In the first step of this process, spent LIBs are deconstructed into cells. The cells are discharged, then physically separated into constituents of cathode, anode, and casing. At the laboratory scale, the separation is manual. To estimate the energy intensity of the discharging step, we adopt the intensity we described in Section 3.9, 0.034 mmBtu/ton battery, which may be an overestimate because it includes three charge/discharge cycles. To translate this energy to an energy intensity of lithium recovered in the hydrometallurgical process, we use Equation 12.

$$EI_{Li,R} = \frac{a_{cathode} EI_{discharge}}{f_{cell} f_{Am} f_{Am,Li} f_R} \quad 12$$

Where $EI_{Li,R}$ is the energy intensity of the discharge step in units of mmBtu/lb recovered Li;
$a_{cathode}$ is the mass allocation factor for the active material (0.52);
$EI_{discharge}$ is the energy intensity of the cycling step in battery manufacturing (0.034 mmBtu/ton battery);
f_{cell} is the fraction of the battery mass made up of cells (0.67) (Nelson et al. 2011);
f_{AM} is the fraction of active material per mass of cell (38%) (Li et al. 2010);
$f_{AM,Li}$ is the fraction of lithium in the active material (cathode) (7%); and
f_R is the fraction of lithium that is recovered (95%).

The discharging cells comprise the casing, cathode (active materials and aluminum foil), copper, graphite, electrolyte, and separator. We assume the makeup of these laptop cells is similar to that of vehicle cells. BatPaC parameters were used to determine the mass ratio of cathode to cell, which is $a_{cathode}$ in Equation 12. The mass of active material in the spent LIBs was 380 g.

The resulting purchased energy intensity is contained in Figure 11, along with energy intensities for other steps in this process.

After discharging, the copper sheet and graphite of the anode are manually (at the laboratory scale) separated from the cathode and the casing. The cathode is soaked in warm NMP (100°C) to separate it from the aluminum foil. To determine the energy intensity for this step, we use Equation 13.

$$EI_{Soak} = \frac{a_{AM} \Delta T}{m_{AM} f_{AM,Li} \eta} \sum C_{p,i} m_i \quad 13$$

Where EI_{Soak} is the energy intensity of the NMP soaking stage;
a_{AM} is the allocation ratio for the active material (0.87);
ΔT is the change in temperature (75°C);
η is the efficiency of the natural gas boiler that is providing steam to heat the vessel (80%);
m_{AM} is the mass of active material;
$C_{p,i}$ is the heat capacity of either NMP (2.1 J/g °C), the active material (1.0 J/g °C), or aluminum (0.90 J/ g °C); and

m_i is the mass of NMP, the active material, or the aluminum.

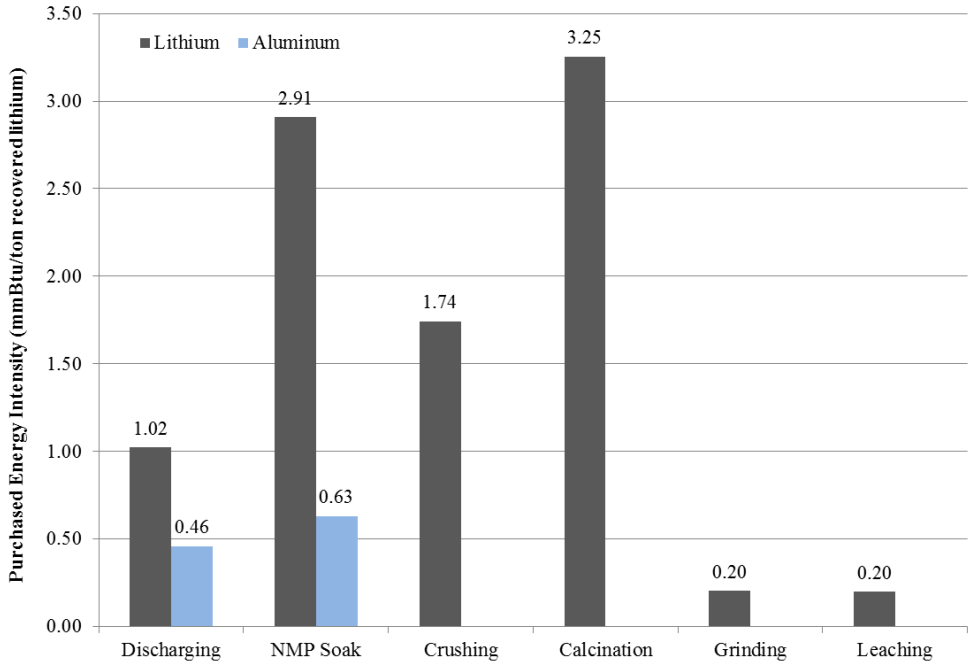


FIGURE 11 Purchased Energy Intensity of Hydrometallurgical Process

We assumed a mass ratio of NMP to active material of 1:1 and used the mass ratio of aluminum foil to active material (0.2) to calculate m_i values. The heat capacity of the active material is based on solid compound heat capacity data (Perry et al. 1999). Further, we assume NMP losses are low, 0.05% as in the battery assembly process (Section 3.9), because residual NMP filtered from the active material can be reused.

To estimate energy consumed in the next two steps of the hydrometallurgical recycling process, we rely on energy consumption data for similar steps in common industrial processes. We take the simple average of these energy intensities; we intend to update the analysis with more specific data as they become available.

After soaking, the active material undergoes crushing in a planetary ball mill. To estimate the energy intensity of this step and the grinding step that precedes leaching, we averaged the energy intensities of grinding steps in 12 industrial processes (Brown et al. 1996), listed in Table 29.

TABLE 29 Energy Intensity for Grinding Steps in Industrial Processes[a]

Manufacturing Process	Grinding Step Energy Intensity (MJ/kg)
TiO_2 via the chloride process	0.09
TiO_2 via the sulfate process	0.12
ZnO via the electrothermal process	0.02
Al_2O_3	0.03
Phosphoric acid via the wet process	5.40
Phosphoric acid via the oxidation method[b]	0.02
Superphosphate fertilizer	0.45
Gypsum products	0.04
Electrometallurgical alloys	0.05 0.01c[b]
Primary aluminum	9.05[d]
Average	1.28

[a] Source: Brown et al. 1996
[b] The rock processed in the oxidation method is sintered before crushing, rendering the crushing step less energy intensive than in the wet process.
[c] The second crushing step in this process handles smaller particles and has a lower energy intensity than the first crushing step in this process.
[d] Coke and pitch are crushed in this step at 24°C.

For the crushing step, we calculated the energy intensity per ton of recovered lithium by dividing the energy intensity per ton of total material by the fraction of lithium in the active material (7%) and again by the recovery efficiency (95%). For the second grinding step, we used the stoichiometric ratio of lithium in $LiCoO_2$ (0.07 ton Li/ton $LiCoO_2$) and the recovery efficiency to convert the energy intensity per mass of active material to a basis of per mass of recovered lithium.

For these steps and all subsequent steps, we allocated lithium's share of the total energy intensity based on the ratio of the mass of output lithium to the total metal output from the leaching step, 0.11.

The next step in the process is calcination at 1,300°F. This step burns off carbon and PVDF. To select an energy intensity for the calcining step, we plotted the energy intensities of the calcining step in six industrial processes (Brown et al. 1996). In general, these data illustrate increasing energy with increasing temperature. We used an energy intensity consistent with the trend in the data at 1,300ºF as a best value, 2.0 mmBtu/ton (shown in Figure 12 as a hollow square). Calcining processes also consume electricity (Brown et al. 1996). We adopted the average electricity consumption of the processes in Figure 12: 0.08 mmBtu electricity/ton.

The subsequent leaching step involves reduction of the cobalt metal to a more soluble divalent form by hydrogen peroxide then subsequent chelation of the cobalt and lithium metals with the organic acid (Li et al. 2012). The lithium is already in a soluble, monovalent form and we assume that manganese would behave similarly to cobalt if the cathode material were $LiMn_2O_4$. We referenced the energy intensity of the leaching step in two industrial processes in selecting a value to use in our analysis (Brown et al. 1996). Table 30 contains the data for these two processes and the average value, which we adopted (despite the small sample size) in the absence of other data.

TABLE 30 Energy Intensity for Leaching Steps in Industrial Processes[a]

Manufacturing Process	Energy intensity (mmBtu/ton)
Potash via the flotation method	0.14[b]
Secondary aluminum	0.10
Average	0.12

[a] Source: Brown et al. 1996.
[b] Assumes consumed steam (0.11 mmBtu/ton) provided via an 80% efficient natural gas boiler.

Figure 11illustrates the purchased energy intensity of each process step per mass of lithium and aluminum recovered. Energy intensities per mass of aluminum were calculated from the lithium intensities and the mass ratio of aluminum to active material (0.2). These intensities are not additive, but they reflect the total energy consumed in the process steps allocated to each material. The shares of natural gas and electricity for the overall process are 66% and 34%, respectively.

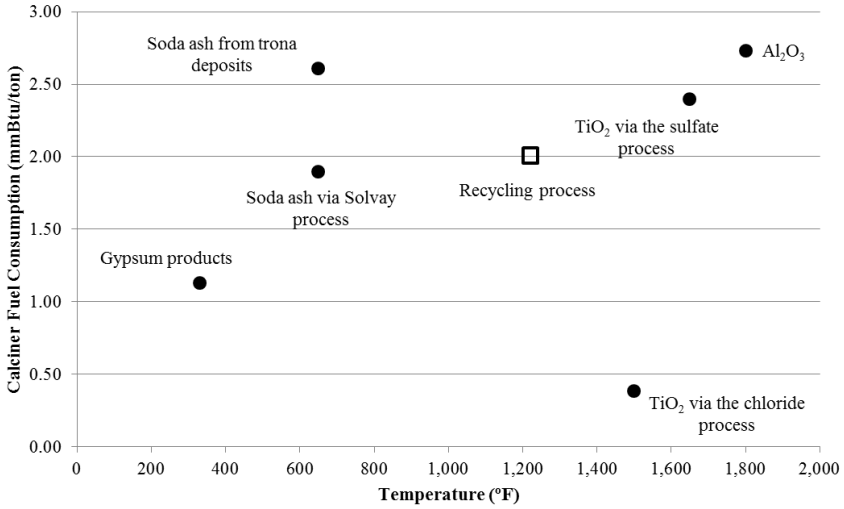


FIGURE 12 Industrial and Selected Energy Intensities for Calcining (Source: Brown et al. 1996)

Another key aspect of the hydrometallurgical process is the material intensity and associated energy and emissions burdens. The process consumes hydrogen peroxide and citric acid in

addition to NMP, as described earlier. Figure 13 depicts how these materials are produced before they are used in the recycling process.

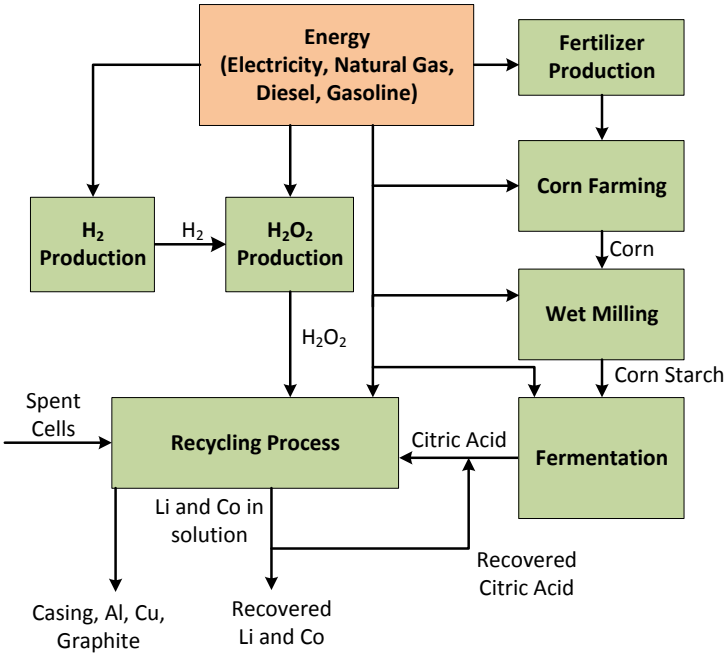


FIGURE 13 Production Pathways of Oxidant and Leachant for Recycling Process

We began with the peroxide and determined its consumption based on laboratory data (Li et al. 2010), as Table 31 details.

TABLE 31 Hydrogen Peroxide Intensity of Acid Leaching Step

Acid	Mass Powder (g)	H_2O_2 Volume (L)	H_2O_2 Concentration (mol/L)	Material Intensity (g H_2O_2/g recovered lithum)
Citric	20	0.01	9.8	2.5
Malic	20	0.02	9.8	5.0
Aspartic	10	0.04	9.8	20

We obtained material and energy flow data for hydrogen peroxide production (Althaus et al. 2007), shown in Table 32. We assumed that steam was produced through the combustion of natural gas, the energy content of which we calculated by determining the enthalpy of steam at

the process conditions (45°C, 53 psia), 189 kJ/kg. We assumed that the natural gas is combusted in an industrial boiler with an efficiency of 80%.

The production of hydrogen peroxide consumes hydrogen, and we incorporated the production and the inherent energy of this feedstock into the analysis. Energy and emissions data for hydrogen production were from GREET (Argonne National Laboratory 2011c) for a central plant with a natural gas feedstock.

TABLE 32 Energy and Feedstock Intensity for H_2O_2 Production from Hydrogen[a,b]

Energy Carrier/Feedstock	Energy intensity (mmBtu/ton)
Electricity	1.7
Residual Oil	0.21
Natural gas	2.2
Steam (included in natural gas)	0.26
Hydrogen	6.8

[a] Sources: Althaus et al. 2007; Argonne National Laboratory 2011c.

[b] Anthraquinone is also used in the production of hydrogen peroxide, but it is regenerated during the process with only a small percentage replenished (Althaus et al. 2007). We do not include it here.

To calculate the contribution of citric acid production to the overall recycling process energy consumption, we first adopted energy consumption and emissions data for the production of corn from the GREET model (Argonne National Laboratory 2011c), as shown in Table 33. Because we were unable to find energy intensity data specifically for citric acid production from corn, we adopted the energy intensity and yield (2.67 gal ethanol/bushel corn) of ethanol production from the wet-milling process from GREET. We modified this yield and intensity to account for the difference in carbon content between ethanol (2 mol C/mol) and citric acid (6 mol C/mol). The resulting energy consumption values are listed in Table 33.

Note that the production energy values are viewed as surrogate values because there are differences in the fermentation process used to produce ethanol versus the process used to produce citric acid. To produce citric acid, the fermenting organism is *Aspergillus niger* mold (Malveda et al. 2009); *Saccharomyces Cerevisae* is used in the fermentation process for ethanol production. Second, the fermentation step in citric acid production may be energy intensive (Malveda et al. 2009), especially if submerged fermentation is used. This technology dominates in the United States, but a less-energy-intensive surface-pan process is more commonly used in less-industrialized countries. Finally, once formed, the citric acid must be separated from solution by either a process that consumes lime and sulfuric acid or a liquid extraction process (Kroschwitz and Seidel 2004). Although the energy consumption value for the corn-to-ethanol-

via-wet-milling pathway includes some separation steps, it does not include those that are specific to citric acid production.

TABLE 33 Energy Intensity Values for Citric Acid[a]

	Corn Production and Distribution[a] (mmBtu/ton)	Fermentation (mmBtu/ton)	Total (mmBtu/ton)
Total Energy	4.0	26	30
Fossil Fuels	3.9	11	15
Coal	0.5	2.9	3.4
Natural Gas	2.0	8.2	10
Petroleum	1.3	0.07	1.4

[a] Source: Argonne National Laboratory 2011c.
[b] Includes fertilizer use, energy to harvest corn, and corn transportation to mill.

We based our calculation of the amount of citric acid the recycling process consumes on stoichiometry. We assumed that each of the acid's three carboxylic acid groups could form a chelate with a metal ion (lithium or cobalt). Because there are two metal ions that can be released from the active material $LiCoO_2$ and three carboxylic acid groups in citric acid, the molar ratio of citric acid to active material is 2:3. We assumed citric acid is fed at a 10% molar excess, resulting in a mass ratio of 21.4 ton citric acid/ton recovered lithium. This methodology simplifies the potentially complex nature of chelate formation, which can take several forms given that citric acid is a multidentate ligand. The typical metal:ligand ratio, however, is 1:1 (Kroschwitz and Seidel 2004). We assumed that 90% of the consumed organic acid is recovered and reused. We do not account for disposing or treating the waste acid.

The recycling process emits CO_2 from the combustion of carbon and PVDF. We calculated these emissions by using Equation 14.

$$E_{CO_2} = \frac{f_i R_i MW_{CO_2}}{MW_t R_{CO_2} f_{AM} f_{AM,Li} f_R} \quad (14)$$

Where E_{CO2} is CO_2 emissions from the calcining step (kg/kg recovered lithium);
R_i is the molar ratio of carbon in carbon (1) or PVDF (2 mol C/mol PVDF);
MW_{CO2} is the molecular weight of CO_2 (44 g/mol);
MW_i is the molecular weight of PVDF (107,000 g/mol [Hester et al. 2002]) or carbon (12 g/mol); and
R_{CO2} is the number of moles of carbon in CO_2.

We allocated these emissions to lithium by using the above-described mass-based allocation factor of 0.11.

We assumed that the recovered lithium can be recovered through precipitation with sodium carbonate and separation from cobalt-containing compounds. The subsequent Li_2CO_3 can be roasted with Mn_3O_4, as described in Section 3.3 to yield $LiMn_2O_4$ that can be used in batteries. Recovered aluminum could also be processed and incorporated into new batteries in a closed-loop recycling scenario.

3.10.2 Pyrometallurgical Recycling Process

Umicore has developed a smelting process (Figure 14) in which batteries, which may be dismantled to the module level, are fed to a high-temperature shaft furnace along with a slag-forming agent that typically includes limestone, sand, and slag. The shaft furnace has three heating zones. In the first, called the pre-heating zone, temperatures are below 300ºC. This lower temperature reduces explosion risks. In this stage, the electrolyte slowly evaporates. The next zone is called the plastics pyrolizing zone and operates at about 700ºC. The burning of the battery's plastics helps maintain the high operating temperature and reduces the overall energy consumption of the smelting step. The last zone is the smelting and reducing zone, where the metallic material transforms to a slag containing lithium, aluminum, silicone, calcium, and some iron. If manganese is present in the cathode material, it will also go into the slag. In addition, an alloy with copper, cobalt, nickel, and some iron forms. This step may be heated by a plasma torch and can reach temperatures between 1,200 and 1,450ºC. Gases leaving the smelter are treated in a post-combustion chamber heated to above 1,150ºC with a plasma torch. It is critical in this stage to capture halogens from the electrolyte through injection of calcium- or sodium-containing products. Alternatively, ZnO can be used to achieve this capture and avoid formation of dioxins or furans. Additional gas clean-up steps are also necessary.

The fate of metals is the key to this process. Importantly, aluminum is not recovered. Lithium is entrained in the slag; it is not economical or energy efficient to recover it. Slag can be used as a beneficial aggregate in concrete. The alloy undergoes two leaching steps that recover copper and iron, likely as salts. To recover cobalt, HCl is added to the process in a solvent extraction step, yielding cobalt chloride ($CoCl_2$). This compound is oxidized to cobalt oxide (Co_3O_4) then fired with Li_2CO_3 to yield $LiCoO_2$ which may need further treatment before it can be used in new batteries. Nickel can also be recovered as nickel hydroxide ($Ni[OH]_2$) from additional processing steps after solvent extraction.

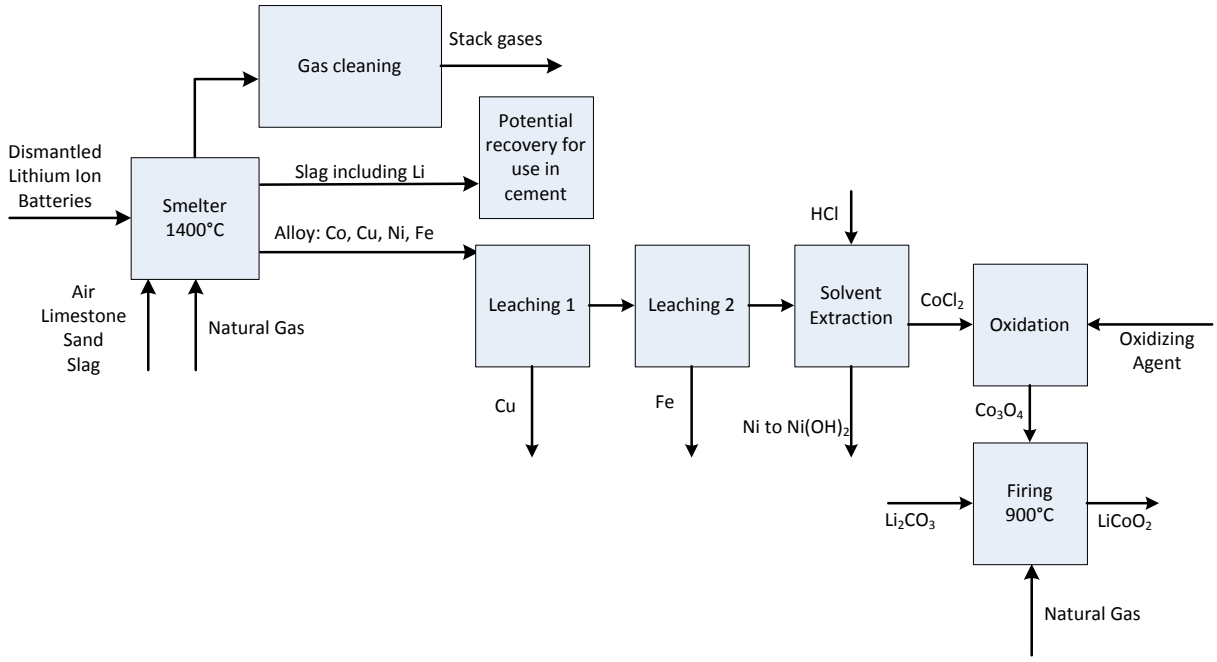


FIGURE 14 Pyrometallurgical Recovery Process (Source: Tytgat 2011)

Key parameters for this process are listed in Table 34, along with their sources.

TABLE 34 Key Parameters for Pyrometallurgical Process

Parameter	Value	Source
Input energy per one ton battery	0.69 mmBtu	Umicore
Mass fraction of cobalt in battery[a]	0.14	Umicore Patent (Cheret & Santen 2007)
Limestone feed rate	0.86 ton limestone/ton cobalt	
Composition of alloy	29% Co/15% Cu/6% Ni/51% Fe	
Energy intensity of leaching steps	0.12 mmBtu/ton alloy	(Brown et al. 1996)
Energy intensity of firing step	2.0 mmBtu/ton fed material	
Ratio of moles Li_2CO_3 to moles Co_3O_4 in firing step	3:2	Stoichiometry

[a] Lithium-ion battery chemistry unspecified in the patent cited.

To determine the energy intensity of the smelting step allocated to cobalt, we used Equation 15. (The remaining energy consumed would be allocated to the other metals in the alloy.)

$$\boldsymbol{EI_{smelt,Co} = \frac{Q_{smelt}}{f_{Co,batt}} \times m_{Co}} \qquad 15$$

Where $EI_{smelt, Co}$ is the energy intensity of the smelting step (mmBtu/ton cobalt);
Q_{smelt} is the energy input per mass of battery (0.69 mmBtu/ton battery) (Caffarey 2009–2012);

$f_{Co,\ batt}$ is the mass fraction of cobalt in the fed batteries (0.14) (Cheret and Santen 2007); and m_{Co} is the mass fraction of cobalt in the alloy (0.29) (Cheret and Santen 2007).

We calculated the energy intensity of the leaching steps with Equation 16.

$$\boldsymbol{EI_{leach,Co} = \frac{EI_{leach}}{m_{Co}} \times (a_{L1} + a_{L2})} \quad 16$$

Where $EI_{leach,\ Co}$ is the energy intensity of the leaching steps allocated to cobalt (mmBtu/ton cobalt);
EI_{leach} is the energy intensity of industrial leaching (0.12 mmBtu/ton alloy) (see Section 3.10.1);
a_{L1} is the mass allocation ratio for cobalt for the first leaching step (0.86);
a_{L2} is the mass allocation ratio for cobalt for the second leaching step (0.41).

We assumed the solvent extraction step consumes a negligible amount of energy but includes the burden of HCl production for this step. We used the energy consumption for HCl production described in Section 3.1.3 and assumed a stoichiometric level of consumption at 0.74 ton HCl/ton $LiCoO_2$. Similarly, we assumed that the oxidation step requires very little energy and occurs at room temperature. However, an oxidizer is required, which we assumed is hydrogen peroxide (H_2O_2) provided at a stoichiometric ratio. In the firing step, Li_2CO_3 is also provided at a stoichiometric ratio. Material and energy burdens for this process are summarized in Table 35. We assumed that natural gas is the only process fuel and that it is burned in a boiler with 80% efficiency for the leaching and firing steps. We assigned emission factors for natural gas combustion in a calciner to the smelting step.

TABLE 35 Purchased Energy and Material Consumption during the Smelting Process

	Energy Intensity		
Process Step	mmBtu/ton cobalt	mmBtu/ton $LiCoO_2$	Material Intensity
Smelting	1.45	0.87	0.86 ton limestone/ton cobalt or 0.51 ton limestone/ton $LiCoO_2$
Leaching	0.52	0.31	
Solvent Extraction	0	0	0.74 ton HCl/ton $LiCoO_2$
Oxidation	0	0	0.23 ton H_2O_2/ton $LiCoO_2$
Firing	8.0	2.4	0.38 ton Li_2CO_3/ton $LiCoO_2$
Total	9.9	3.6	

We developed process CO_2 emissions for the smelting step by assuming that all carbon-containing materials in the battery are completely combusted to CO_2. These products and their carbon content are listed in Table 36.

TABLE 36 Carbon-Containing Components in LIBs and their Carbon Contents

Component	g C/g component
Polyethylene terephthalate	0.63
Polypropylene	0.86
Polyethylene	0.92
Carbon/graphite	1.0
Ethylene carbonate	0.41
Dimethyl carbonate	0.40
Glycol	0.39
PVDF	0.36

We used these parameters and the average mass fraction of each of these components in the three batteries examined in this study (Table 2) in Equation 17 to calculate CO_2 process emissions.

$$\boldsymbol{E_{CO2}} = \frac{\boldsymbol{m_{battery} R_{CO2}}}{\boldsymbol{m_{cobalt\ out}}} \sum \boldsymbol{m_i R_{C,i}} \times \frac{\boldsymbol{454\ g}}{\boldsymbol{lb}} \times \frac{\boldsymbol{2000\ lb}}{\boldsymbol{ton}} \quad 17$$

Where $m_{battery}$ is the mass of battery input to the smelter (1 g);
$m_{cobalt,out}$ is the output mass of cobalt from the smelter (0.011 g);
m_i is the component mass fraction in the battery (Nelson et al. 2011); and
$R_{C,i}$ is the mass fraction of carbon in the component.

This equation yields carbon process emissions of 1.5 million g CO_2/ton cobalt.
We also account for the decomposition of limestone in the smelting step to yield 342,144 g CO_2/ton cobalt.

3.10.3 Intermediate Physical Recycling Process

The intermediate physical recycling processes (Figure 15) recovers Li_2CO_3, which is farther along in the material production chain (Figure 1) than the lithium salt recovered in the hydrometallurgical process, as described in Section 3.10.1. In this process, batteries undergo physical processes that break them apart into smaller pieces. A shaker table separates out mixed plastics and metals. Filtering of the second stream leaving the hammermill yields mixed metal oxides and carbon. The liquid stream leaving the filter press is dewatered to some extent, then mixed with soda ash to precipitate Li_2CO_3, which is subsequently filtered from solution. The success of this technology in recovering Li_2CO_3 could depend on co-location with a primary lithium plant to increase the concentration of lithium in the process. In our analysis, we assumed that the process has sufficient lithium to enable Li_2CO_3 production.

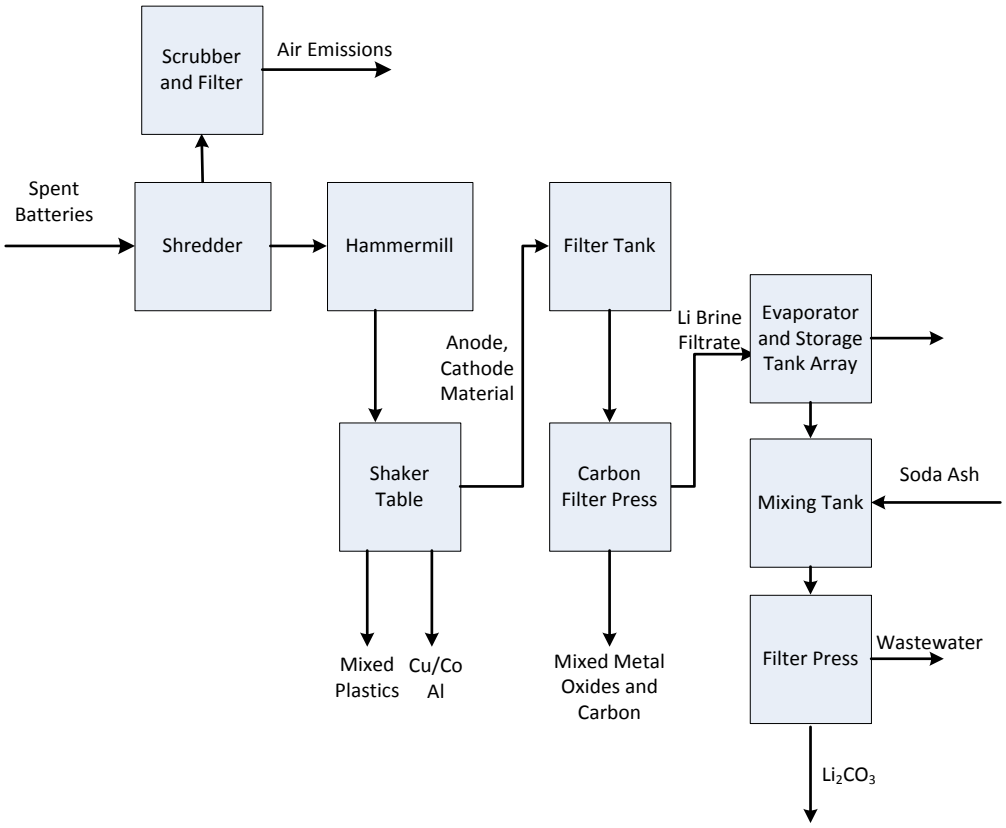


FIGURE 15 Intermediate Recycling Process Flowchart (Coy 2008–2012)

To model this process, we obtained data from Toxco, which uses this technology in Trail, British Columbia (Coy 2008–2012). The material flows in this process are listed in Table 37. All data except the soda ash input, which is assumed to be at a stoichiometric ratio, were provided by Toxco.

TABLE 37 Material Flows in the Intermediate Physical Recycling Process

Parameter	Mass flow (ton/ton Li_2CO_3)
Input	
Battery	33.3
Soda ash input	2
Output	
Mixed plastics	1.33
Copper	8.33
Aluminum	7.00
Mixed metal oxides and carbon	1.67

We calculated energy intensities for this process on a per-mass-of-Li_2CO_3 and per-mass-of-aluminum basis. Beginning with Li_2CO_3, we adjusted the energy consumption of the shredder and hammermill (0.54 mmBtu/ton material) to a per-ton-Li_2CO_3 basis with Equation 18. Note that the fraction of active material in the streams entering and leaving these process steps are equal, so mass allocation of the energy intensity effectively multiplies the value by one.

$$\boldsymbol{EI_{Shred,Li2CO3} = \frac{EI_{Shred}}{f_{Li}} \times r_{Li}} \quad 18$$

Where $EI_{Shred,\ Li2CO3}$ is the energy of the shredding and hammermill steps allocated to Li_2CO_3;
EI_{shred} is the unallocated energy consumption of these steps (0.54 mmBtu/ton material);
f_{Li} is the mass fraction of lithium in $LiMn_2O_4$ (0.04); and
r_{Li} is the mass fraction of lithium in Li_2CO_3 (0.18).

In the case of aluminum, the energy intensity of the shredding and hammermill step is 0.54 mmBtu/ton aluminum. The aluminum is subsequently separated from plastics, copper, anode and cathode material, and cobalt by means of a shaker table. Energy consumption for the shaker table was estimated at 0.003 mmBtu/ton, which is the energy consumption of a belt conveyor used in a material recovery facility (Nishtala and Solano-Mora 1997). This approach could underestimate the energy the shaker table consumes because it may move more than a belt conveyer. We applied mass allocation to this intensity to calculate a value of 0.001 mmBtu/ton aluminum.

Returning to Li_2CO_3, we calculated the energy intensity of two filtration steps that precede its recovery from the process, but we considered that the energy consumption of the intermediate steps in the tanks is negligible. For the filter press, we adopted a best energy intensity value based on data in Brown et al. (1996) for filtration of high-solids streams. (The stream entering the first filter press in the Toxco process could have a solid-to-liquid ratio of 5:1.) In the manufacture of cellulosic fibers, a stream that is 98% solids requires 0.26 mmBtu/ton to filter. Filtering a stream with 83% solids in the manufacture of synthetic rubber consumes 0.34 mmBtu/ton. In our analysis of intermediate recycling, we used a value of 0.3 mmBtu/ton for the filter press steps. For the first filter press, we applied mass allocation to yield a value of 7×10^{-4} mmBtu/ton Li_2CO_3. The second filter press has a single output stream of Li_2CO_3, so the energy burden falls fully on this product.

The energy intensities for each step of the intermediate recycling process are displayed in Table 38. Note that the output Li_2CO_3 could be either converted to $LiCoO_2$ by the firing step in the pyrometallurgical process or to $LiMn_2O_4$ from roasting the carbonate with Mn_2O_3, as described in Section 3.3.

TABLE 38 Purchased Energy Consumption during Intermediate Recycling Process

Equipment	mmBtu/ton Li_2CO_3	mmBtu/ton Aluminum
Shredder and hammermill	2.6	0.54
Shaker table	0.08	7.0×10^{-4}
Carbon filter press	6.9×10^{-4}	
Filter press	0.03	
Total	2.7	0.54

3.10.4 Direct Physical Recycling Process

The direct physical recycling process recovers battery materials for reinsertion into the battery supply chain with little or no additional processing. Notably, this process has not yet been commercialized. This process for batteries with $LiCoO_2$ as the active material is illustrated in Figure 16 (Sloop and Parker 2011). We assume the technology would work similarly if $LiMn_2O_4$ were the active material.

First, batteries are discharged and disassembled to the cell level. Next, breached discharged cells are placed in a container to which CO_2 is added. The temperature and pressure are raised to bring CO_2 above its critical point. The supercritical carbon dioxide ($SCCO_2$) extracts the electrolyte (EMC, DC, $LiPF_6$) from the cells. A solubility enhancer (such as alkyl esters) and a Lewis base (such as ammonia or pyridine) may be added to assist with electrolyte extraction. A lithium-containing compound could also be added in this step to increase the cell's lithium content. The supercritical fluid can then be removed from the extraction chamber. When the temperature and pressure are reduced, the electrolytic compounds will separate from the gaseous CO_2. After further processing, they may be recycled and used again in batteries. It is unclear what types of further processing would be necessary if solubility enhancers and Lewis bases were to be added to the $SCCO_2$.

The cells, devoid of electrolyte, undergo pulverization or other size-reduction steps, possibly in the absence of water or oxygen to avoid contamination of materials. Subsequently, the cell components are separated through techniques that exploit differences in electronic conductivity, density, or other properties. No step is taken to separate the PVDF binder from the active materials, which may prove to be a significant barrier for this process. Cathodic materials may need to undergo relithiation prior to reuse in batteries.

This process has the advantage that all battery components, including aluminum, are recovered and can be reused in most cases after further processing. There is some question, however, as to whether the recovered cathodic material will perform as well as virgin cathodic material, which could have implications for battery power and lifetime.

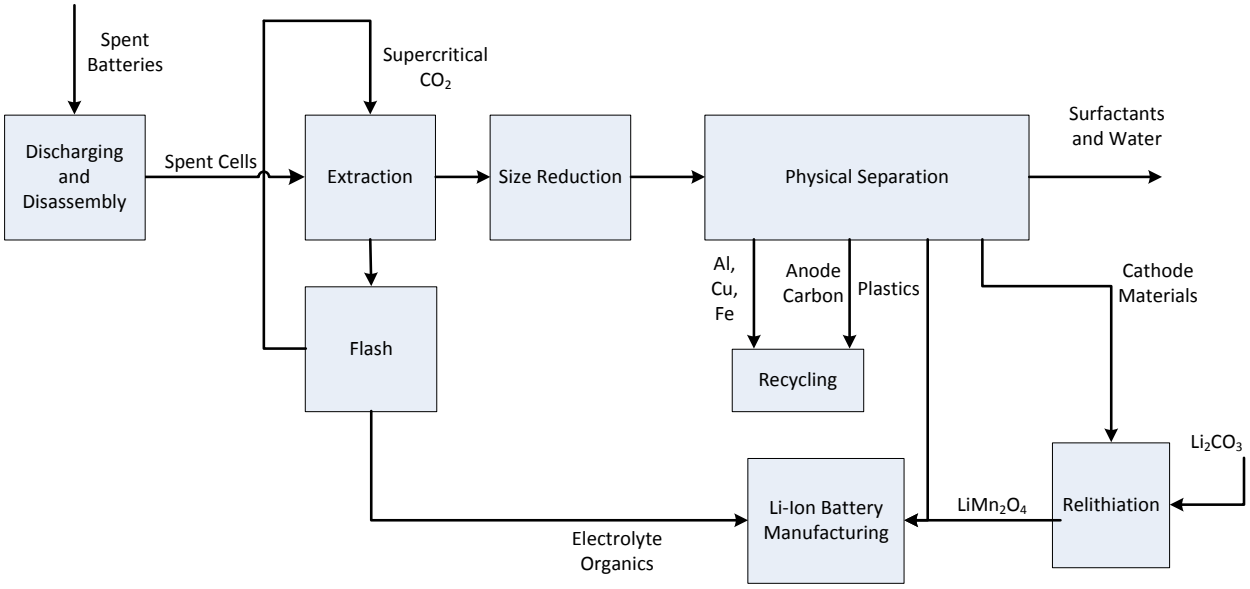


FIGURE 16 Direct Recycling Process

The technology developers have supplied some data on this process (Ellis and Hohn 2009–2012; Sloop 2009–2012) that, together with engineering calculations, have permitted calculation of material and energy flows. The energy and material intensity of the first step ($SCCO_2$) depend on the solubility of the organic constituents of the electrolyte, EC and DMC, in $SCCO_2$. In turn, their solubility depends on the process conditions. We assume that the pressure of the extraction step is 120 bar (Sloop and Parker 2011). Although we could not locate solubility data specific to these compounds, we obtained data for a proxy compound, cyclohexanone (Gupta and Shim 2006). Cyclohexanone is cyclic, with a ketone group like that of EC. The data in Table 39 demonstrate that its chemical formula and molecular mass are reasonably similar to those of the organic compounds in the electrolyte.

TABLE 39 Properties of Cyclohexanone and Electrolyte

Compound	Formula	Molecular weight (g/mol)
Ethylene carbonate	$C_3H_4O_3$	88.0621
Dimethyl carbonate	$C_3H_6O_3$	90.08
Cyclohexanone	$C_6H_{10}O$	98.14

At 136°C and 120 bar, the mole fraction of cyclohexanone in the vapor phase is $19{,}700 \times 10^{-6}$ (Gupta and Shim 2006). We calculated the required feed ratio of $SCCO_2$ by using Equation 19.

$$r_{SCCO2} = \frac{1}{y \times \frac{98.14\ g}{1\ mol\ cyclohexanone} \times \frac{1\ mol\ CO_2}{44\ g}} \quad (19)$$

In this equation, r_{SCCO2} is the feed ratio of CO_2 (23 ton $SCCO_2$/ton organic) and y is the mole fraction of cyclohexanone in the vapor phase. This feed ratio may be underestimated because the process temperature is below 136ºC.

The average EC and DMC content of the cells is 12-14%. We used this percentage to calculate that, per ton of processed battery (which, in our study, consists of 96 cells), 2.2 ton of $SCCO_2$ must be fed. To calculate the energy required to compress the $SCCO_2$ to the process pressure (120 bar), we used the compression calculations in GREET (Argonne National Laboratory 2011c) and the parameters listed in Table 40. We assumed that in an industrial process, the CO_2 would be recovered through a pressure lowering (flash step) in which the organics leave solution. The recovered CO_2 is then repressurized. Some make-up CO_2 may be required, but because CO_2 is typically created as a by-product of another process (e.g., hydrogen production or ethanol production) (Suresh et al. 2007), we neglect any energy demand for its generation.

TABLE 40 Compression Energy Demand Calculation Parameters

Parameter	Value
Inlet pressure (psia)	100
Outlet pressure (psia)	1,740
Inlet Temperature (°F)	70
Specific Heat Ratio	1.32
Compression ratio per stage	2.1
Number of compression stages	4
Adiabatic compressor efficiency	65%
Compressibility factor (z) (Perry et al. 1999)	0.81
Theoretical Energy (kWh/kg)	0.16
Shaft energy (kWh/kg)	0.16
Electric motor efficiency	95%
Electric energy (kWh/kg)	0.17
Electric energy (mmBtu/ton $SCCO_2$)	0.5

We calculated the energy intensity of the extraction step on a per mass of $LiMn_2O_4$ basis from Equation 20.

$$EI_{extract,i} = \frac{R_{SCCO2} \times EI_{compress} \times m_{EC,DMC}}{f_i} \times m_i \quad (20)$$

Where $EI_{extract, LiMn2O4}$ is the energy consumed by the extraction step (mmBtu /ton $LiMn_2O_4$);
R_{SCCO2} is the feed rate of $SCCO_2$ (23 ton $SCCO_2$/ton EC and DMC);
$EI_{compress}$ is the energy intensity of compressing CO_2 (0.5 mmBtu/ton $SCCO_2$);

$m_{EC, DMC}$ is the mass fraction of EC and DMC in the cell with electrolyte (0.14);
f_i is the mass fraction of Al or $LiMn_2O_4$ in the cell with electrolyte (0.09, 0.39); and
m_i is the mass fraction of Al or $LiMn_2O_4$ in the battery after electrolyte extraction (0.11, 0.45).

The energy intensity of the size reduction and physical separation steps is 0.22 and 0.02 mmBtu/ton cell, respectively (Ellis and Hohn 2009–2012; Sloop 2009–2012). These values were converted to per-aluminum or -$LiMn_2O_4$ bases by multiplying by m_i/f_i. Table 41 summarizes the energy intensity of the direct recycling process for both $LiMn_2O_4$ and aluminum. They are equal because m_i/f_i is equivalent for the two cell constituents. In addition, we adopted the battery discharge energy from Section 3.9.

TABLE 41 Purchased Energy Consumption during Direct Recycling Process

Step	mmBtu/ton $LiMn_2O_4$ or Aluminum
Discharging	0.12
Extraction	1.95
Size Reduction	0.25
Physical Separation	0.02
Total	2.34

Finally, we assume that 5% of the lithium content in the battery must be provided for the relithiation step, resulting in a Li_2CO_3 demand of 0.01 ton Li_2CO_3/ton $LiMn_2O_4$ (Ellis 2012).

It is worth reiterating that this process is still under development. As more data become available, we will revisit our analysis of direct physical recycling. The current analysis serves as a starting point to analyze process energy and environmental burdens.

3.10.5 Recycling Process Summary

Comparing recycling processes directly is difficult given that they produce different materials that fall in different tiers in the battery supply chain. The direct recycling process, which we assumed can recover $LiMn_2O_4$, has the greatest potential to reduce the energy consumption during the production (from cradle-to-gate) of LIBs. Our preliminary analysis (Dunn et al. 2012) estimates that the total energy consumed in recovering $LiMn_2O_4$ through this process could be four times less than the total energy required to produce virgin $LiMn_2O_4$ using Li_2CO_3 from Chile. We will provide further analyses of these processes and their impact on battery production (materials production and assembly) energy and emissions in our upcoming journal article (Dunn et al. 2012).

4 CONCLUSIONS AND FUTURE WORK

In this report, we describe the development of new and revised material and energy flows for the materials production, assembly, and recycling of an LIB with an active cathode material of $LiMn_2O_4$. An upcoming journal article will analyze these flows (Dunn et al. 2012). Together with use-phase data in GREET, these data enable LCA of batteries for HEVs, PHEVs, and EVs in the GREET model.

We have identified the following research areas to pursue that will improve these data and subsequent LCA of batteries and battery-containing vehicles using GREET.

4.1 MASS INVENTORY OF BATTERY COMPONENTS

We relied on the BatPaC model to develop the inventory of battery components. This model, however, contains basic assumptions about the masses of the TMS and the BMS. In this work, we did not address the TMS beyond incorporating the impacts of the coolant fluid, glycol. In future work, we will seek to include the impacts of the TMS. BatPaC also assumes that the BMS is a set percentage of battery mass. We have improved upon this assumption with direct measurements of BMS and battery circuitry. There is still, however, room for an improved estimate of BMS mass.

In addition, BatPaC assumes a certain design for the battery, cell, and module housing that results in high aluminum content in the battery. Alternative housing designs may use more plastic, thereby altering the breakdown of plastics and metals in the battery. Recently, the GM Volt required a retrofit that added extra steel around the battery pack, a sensor to keep track of coolant levels, and a bracket to prevent coolant tank leaks (Priddle 2012). We will consider alternative cell, module, and battery packaging designs and their effect on the life-cycle impacts of batteries.

4.2 CRADLE-TO-GATE INVENTORIES

The battery component with the highest mass is the cathodic active material. In this report, we consider only one option for this key battery ingredient, $LiMn_2O_4$. BatPaC allows users to model batteries with other cathodic active materials that we would like to pursue, including lithium nickel manganese cobalt oxide ($LiNiMnCoO_2$) and lithium iron phosphate ($LiFePO_4$).

Further, many techniques are available to produce active material from different building blocks. We will examine these different routes and select several to examine in addition to the one route included in this work ($Li_2CO_3 + Mn_2O_3 = LiMn_2O_4$).

The energy intensity of battery assembly is very uncertain for the reasons discussed in Section 3.9. We will continue to pursue data for this step. Similarly, energy consumption during battery recycling is an uncertain parameter. At times, our analysis relies on laboratory data and surrogate

values for similar unit processes; we will incorporate data specific to battery recycling processes as they become available. The materials obtained as outputs from the recycling processes may require additional processing not considered in this work to bring them up to a level of performance suitable for inclusion in batteries. We will stay abreast of developments in recycling technologies, which may change as battery chemistries change.

Finally, material acquisition and LIB assembly are both very international processes; we have begun to reflect that in this work. For example, we only include transport impacts for the cathode material supply chain. However, we have not captured several supply chain features, including battery assembly in Asia, which is the current and likely future scenario (to a large extent). We will examine the impact of supply chain flows through transportation impacts on battery production energy consumption and emissions.

5 REFERENCES

Althaus, H., R. Hischier, M. Osses, A. Primas, S. Hellweg, N. Jungbluth, and M. Chudacoff, 2007, Life Cycle Inventories of Chemicals, Ecoinvent Report Number 8, Swiss Centre for Life Cycle Inventories, Dübendorf, CH.

Argonne National Laboratory, 2011a, BatPaC Model, available at http://www.cse.anl.gov/BatPaC/about.
html, last accessed March 30, 2012.

Argonne National Laboratory, 2011b, Autonomie, available at http://www.autonomie.net/, last accessed March 30, 2012.

Argonne National Laboratory, 2011c, GREET1_2011, available at http://greet.es.anl.gov/, last accessed March 30, 2012.

Beal, M., and E. Linak, 2011, *Chlorine/Sodium Hydroxide*, Chemical Economics Handbook (CEH) Marketing Research Report, SRI Consulting, Zurich, Switzerland.

Boustead, I., 2005a, "Eco-profiles of the European Plastics Industry: Purified Brine," Plastics Europe, Brussels, Belgium.

Boustead, I., 2005b, "Eco-profiles of the European Plastics Industry: Ethylene," Plastics Europe, Brussels, Belgium.

Brown, H., B. Hedman, B., and B. Hamel, 1996, *Energy Analysis of 108 Industrial Processes*, Fairmont Press, distributed by Prentice Hall PTR, Lilburn, GA; Upper Saddle River, NJ.

Burnham, A., M. Wang, and Y. Wu, 2006, *Development and Applications of GREET 2.7 — The Transportation Vehicle-Cycle Model*, Report ANL/ESD/06-5, Argonne National Laboratory, Argonne, IL.

Caffarey, M., 2009–2012, personal communications, Umicore Group, Brussels, Belgium.

Cheret, D., and S. Santen, 2007, *Battery Recycling*, United States Patent 7,169,206, Jan. 30.

Coy, T., 2008–2012, personal communications, Toxco Battery Recycling, Anaheim, CA.

Deng, L., C.W. Babbit, and E.D. Williams, 2011, "Economic-Balance Hybrid LCA Extended with Uncertainty Analysis: Case Study of a Laptop Computer," *Journal of Cleaner Production* **19**, 1198–1206.

DOE: see U.S. Department of Energy

Dunn, J.B., L. Gaines, J. Sullivan, and M. Wang, 2012, "The Impact of Recycling on Cradle-to-Gate Energy Consumption and Greenhouse Gas Emissions of Automotive Lithium-Ion Batteries," *Environmental Science and Technology*, submitted.

EIA: see Energy Information Administration

Ellis, T., 2012, personal communication, Jan. 26, RSR Corporation, Dallas, TX.

Ellis, T., and J. Hohn, 2009–2012, personal communications, RSR Corporation, Dallas, TX.

EMD, 2011, Material Safety Data Sheet for SelectiLyte™ Battery electrolyte LP 71. Gibbstown, NJ. Available at http://www.emdmillipore.com/chemicals, last accessed June 6, 2012.

Energy Information Administration, 2009, *2006 Manufacturing Energy Consumption Survey*. DOE, Washington, D.C., available at http://www.eia.gov/emeu/mecs/contents.html, last accessed Feb. 7, 2012.

Energy Information Administration, 1997, *1994 Manufacturing Energy Consumption Survey*, DOE, Washington, D.C.

EPA: see U.S. Environmental Protection Agency

Espinosa, N., R. García-Valverde, and F.C. Krebs, 2011, "Life-Cycle Analysis of Product Integrated Polymer Solar Cells," *Energy & Environmental Science* **4**, 1547.

European Aluminum Association, 2008, *Environmental Profile Report for the European Aluminum Industry*, April, available at http://transport.world-aluminium.org/uploads/media/1274452909Environmental_Profile_Report_01.pdf, last accessed May 2012.

Gallagher, K., 2011, personal communication, Feb. 24, Argonne National Laboratory, Argonne, IL.

Garrett, D.E., 2004, *Handbook of Lithium and Natural Calcium Chloride their Deposits, Processing, Uses and Properties*, Elsevier Academic Press, Amsterdam; Boston.

Glauser, J., S. Schlag, and C. Funada, 2009, *Hydrochloric Acid*, CEH Marketing Research Report, SRI Consulting, Zurich, Switzerland.

Glauser, J., and Y. Inoguchi, 2011, *Lithium, Lithium Minerals, and Lithium Chemicals*, CEH Marketing Research Report, SRI Consulting, Zurich, Switzerland.

Groves, J., 2011, personal communication, May 11, Chemetall Foote Corporation, Kings Mountain, NC.

Gruber, P., P.A. Medina, G.A. Keoleian, S.E. Kesler, M.P. Everson, and T.J. Wallington, 2011, "Global Lithium Availability a Constraint for Electric Vehicles?" *Journal of Industrial Ecology*, **15**, 760–775.

Gupta, R.B., and J.-J. Shim, 2006, *Solubility in Super Critical Carbon Dioxide*, CRC Press, Boca Raton, FL.

Han, Y.S., H.G. Kim, and K.S. Park, 2003, *Method of Manufacturing Lithium-Manganese Oxide for Use in Lithium Secondary Battery*, United States Patent 6576216, June 10.

Hester, J. F., P. Banerjee, Y.-Y. Won, A. Akthakul, M. H. Acar, A. M. Mayes, 2002, "ATRP of Amphiphilic Graft Copolymers Based on PVDF and Their Use as Membrane Additives," *Macromolecules*, **35**, 7652-7661.

IEA: see International Energy Agency

International Aluminum Institute, 2007, *Life-Cycle Assessment of Aluminum: Inventory Data for the Primary Aluminum Industry — Year 2005 Update*, Sept., London, United Kingdom.

International Energy Agency, 2008, *Report and Updates from Participants of the Meeting on the World's Supply of Lithium*, Paris, France.

International Energy Agency, 2012, "Electricity/Heat in Chile in 2009," available at http://www.iea.org/stats/electricitydata.asp?COUNTRY_CODE=CL, last accessed March 30, 2012.

Kostick, D.S., 2001, *Soda Ash*, United States Geological Survey (USGS) Report, available at http://minerals.usgs.gov/minerals/pubs/commodity/soda_ash/sodamyb01.pdf, last accessed May 2012.

Kroschwitz, J.I., and A. Seidel, 2004, Kirk-Othmer Encyclopedia of Chemical Technology, Wiley-Interscience, Hoboken, NJ.

Li, L., J.B. Dunn, X.X. Zhang, L. Gaines, F. Wu, and R.J. Chen, 2012, Recovery of Metals from Spent Lithium-Ion Batteries with Organic Acids as Leaching Reagents and Life Cycle Analysis," *Journal of Industrial Ecology*, submitted**.**

Li, L., J. Ge, F. Wu, R. Chen, S. Chen, and B. Wu, 2010, "Recovery of Cobalt and Lithium from Spent Lithium Ion Batteries Using Organic Citric Acid as Leachant," *Journal of Hazardous Materials* **176**, 288–293.

Majeau-Bettez, G., T.R. Hawkins, and A.H. Strømman, 2011, Life Cycle Environmental Assessment of Lithium-Ion and Nickel Metal Hydride Batteries for Plug-In Hybrid and Battery Electric Vehicles," *Environmental Science & Technology* **45**, 4548–4554.

Malveda, M.P., H. Janshekar, and Y. Inoguchi, 2009, *Citric Acid*, CEH Marketing Research Report, SRI Consulting, Zurich, Switzerland.

Mitchell, J., 2011, personal communication, July 1, SCS Systems, Houston, TX.
Moneypenney, B., 2011, personal communication, May 11, Dow Kokam, Midland, MI.

Moretz-Sohn Monteiro, J.G., O. Queiroz Fernandes Araújo, and J.L. Medeiros, 2009, "Sustainability Metrics for Eco-Technologies Assessment, Part II: Life Cycle Analysis," *Clean Technologies and Environmental Policy* **11**, 459–472.

National Council for Air and Stream Improvement, 2009, *Environmental Footprint Comparison Tool for Understanding Environmental Decisions Related to the Pulp and Paper Industry*, available at http://www.paperenvironment.org/PDF/SOxNOx/SOxNOx_Full_Text.pdf, last accessed March 30, 2012.

National Renewable Energy Laboratory, 2012, "U.S. Life Cycle Inventory Database Home Page," available at http://www.nrel.gov/lci/, last accessed Feb. 7, 2012.

Nelson, P.A., K.G. Gallagher, I. Bloom, and D.W. Dees, 2011, *Modeling the Performance and Cost of Lithium-Ion Batteries for Electric-Drive Vehicles*, Report ANL-11/32, Argonne National Laboratory, Argonne, IL.

Nevada Department of Conservation and Natural Resources, 2010, *Class II Air Quality Operating Permit*, Permit Number AP1479-0050.02, Chemetall Foote Corporation, Silver Peak, NV.

NCNR: see Nevada Department of Conservation and Natural Resources.

Nishtala, S., and E. Solano-Mora, 1997, Description of the Material Recovery Facilities Process Model Design, Cost, and Life-Cycle Inventory, project report prepared for EPA by North Carolina State University, Raleigh, NC.

Notter, D.A., M. Gauch, R. Widmer, P. Wager, A. Stamp, R. Zah, and H.-J. Althaus, 2010, "Contribution of Li-Ion Batteries to the Environmental Impact of Electric Vehicles," *Environmental Science & Technology* **44**, 6550–6556.

Okada, M., and M. Yoshio, 2009, "$LiMn_2O_4$ as a Large-Capacity Positive Material for Lithium-Ion Batteries," in *Lithium-Ion Batteries Science and Technologies*, M. Yoshio, R.J. Brodd, and A. Kozawa (Eds.), Springer, New York, NY.

Ostermayer, A., and J. Giegrich, 2006a, *Eco-Profiles of the European Plastics Industry: Polyvinyl Chloride (Emulsion Polymerization)*, The European Council of Vinyl Manufacturers (ECVM) and Plastics Europe.

Ostermayer, A., and J. Giegrich, 2006b, *Eco-Profiles of the European Plastics Industry: Polyvinyl Chloride (Suspension Polymerization)*, The European Council of Vinyl Manufacturers (ECVM) and Plastics Europe.

PE Americas, 2010, *Life Cycle Impact Assessment of Aluminum Beverage Cans*, prepared for Aluminum Association, Inc., Washington, D.C. available at http://www.container-recycling.org/assets/pdfs/aluminum/LCA-2010-AluminumAssoc.pdf, last accessed March 30, 2012.

Perry, R.H., D.W. Green, and J.O. Maloney, 1999, *Perry's Chemical Engineer's Platinum Edition, Perry's Chemical Engineers' Handbook*, McGraw-Hill, New York, NY.

Priddle, A., 2012, "U.S. Closes its Investigation into Chevrolet Volt Battery Fires, Accepts GM's Fix," *Detroit Free Press*, available at http://www.freep.com/article/20120120/BUSINESS0101/120120046/Chevy-Volt-battery-fire-investigation-closed, last accessed Feb. 14, 2012.

RCCRMARA: see Republica de Chile Comision Regional del Medio Ambiente de la Region de Antofagasta

Republica de Chile Comision Regional del Medio Ambiente de la Region de Antofagasta 2007, Previsualización de Resolución de Calificación Ambiental (RCA), available at http://seia.sea.gob.cl/documentos/documento.php?idDocumento=2184703, last accessed Feb. 7, 2012.

Research Triangle Institute, 2000, *Lime Production: Industry Profile*, prepared for EPA's Air Quality Standards and Strategies Division, Office of Air Quality Planning and Standards, Innovative Strategies and Economics Group, by Research Triangle Institute, Center for Economics Research, Research Triangle Park, NC, Sept., available at http://www.epa.gov/ttnecas1/regdata/IPs/Lime%20Manufacturing_IP.pdf, last accessed May 2012.

Salt Institute, 2011, "What is Salt? and Other Common Salt Questions," available at http://www.saltinstitute.org/About-salt/Salt-FAQs, last accessed March 8, 2012.

Schlag, S., and A. Kishi, 2011, *Boron Minerals and Chemicals*, CEH Marketing Research Report, SRI Consulting, Zurich, Switzerland.

Singhal, A., and S. Ganesh, 2005, *Nanostructured and Layered Lithium Manganese Oxide and Method of Manufacturing the Same*, United States Patent 6,960,335, Nov. 1.

Sloop, S.E., and R. Parker, 2011, *System and Method for Processing an End-of-Life or Reduced Performance Energy Storage and/or Conversion Device Using a Supercritical Fluid*, United States Patent 8,067,107 B2, Nov. 29.

Sloop, S., 2009–2012, personal communications, OnTo Technology, LLC, Bend, OR.

SQM, 2001, Capitulo 2 Descripcion del Proyecto. Available at http://seia.sea.gob.cl/expediente/expedientesEvaluacion.php?modo=ficha&id_expediente=3521#-1, last accessed May 2012.

Stamp, A., D.J. Lang, and P.A. Wäger, 2012, "Environmental Impacts of a Transition toward E-Mobility: the Present and Future Role of Lithium Carbonate Production," *Journal of Cleaner Production* **23**, 104–112.

Suresh, B., S. Schlag, and Y. Ishikawa, 2007, *Carbon Dioxide*, CEH Marketing Research Report, SRI Consulting, Zurich, Switzerland.

Suresh, B., C. Funada, and Y. Ping, 2010, *Inorganic Potassium Chemicals*, CEH Marketing Research Report, SRI Consulting, Zurich, Switzerland.

Sutter, J., 2007, *Life Cycle Inventories of Petrochemical Solvents*, Swiss Centre for Life Cycle Inventories.

Tagawa, K., and R.J. Brodd, 2009, "Production Processes for Fabrication of Lithium-Ion Batteries," in *Lithium-Ion Batteries Science and Technologies*, M. Yoshio, R.J. Brodd, and A. Kozawa (Eds.), Springer, New York, NY.

The International Council of Forest and Paper Associations, 2005, "Calculation Tools for Estimating Greenhouse Gas Emissions from Pulp and Paper Mills," available at http://www.ncasi.org/support/downloads/Detail.aspx?id=3, last accessed March 30, 2012.

Tytgat, J., 2011, *EV Battery Recycling: Resource Recovery*, presented at Plug-in 2011, July 18–21, Raleigh, NC.

U.S. Census Bureau, 1992, "1992 Economic Census," available at http://www.census.gov/epcd/www/92 result.html, last accessed May 2012.

U.S. Census Bureau, 1997, "1997 Economic Census," available at http://www.census.gov/epcd/www/ econ97.html, last accessed May 2012.

U.S. Census Bureau, 2007, "2007 Economic Census," available at http://www.census.gov/econ/census07/, last accessed May 2012.

U.S. Department of Energy, 2002, *Energy and Environmental Profile of the U.S. Mining Industry*, Washington, D.C.

U.S. Environmental Protection Agency, 2012, RACT/BACT/LAER Clearinghouse (RBLC), available at http://cfpub.epa.gov/RBLC/, last accessed Feb., 2012.

U.S. Environmental Protection Agency, 1998, "Chapter 11: Mineral Products Industry," in *AP 42, Fifth Edition, Volume I*, available at http://www.epa.gov/ttn/chief/ap42/ch11/index.html, last accessed Feb. 7, 2012.

U.S. Environmental Protection Agency, 1993, "Chapter 8: Inorganic Chemical Industry," *AP 42, Fifth Edition, Volume I*, available at http://www.epa.gov/ttn/chief/ap42/ch08/index.html, last accessed Feb. 7, 2012.

USGS: see U. S. Geological Survey

U. S. Geological Survey, 2008, *Mineral Commodity Summaries 2008*.

U.S. Geological Survey, 2010, *Minerals Commodity Summaries 2010*.

Yao, M.A., T.G. Higgs, M.J. Cullen, S. Stewart, and T.A. Brady, 2010, "Comparative Assessment of Life Cycle Assessment Methods Used for Personal Computers," *Environmental Science & Technology* **44**, 7335–7346.



Energy Systems Division
Argonne National Laboratory
9700 South Cass Avenue, Bldg. 362
Argonne, IL 60439-4815

www.anl.gov



Argonne National Laboratory is a U.S. Department of Energy
laboratory managed by UChicago Argonne, LLC